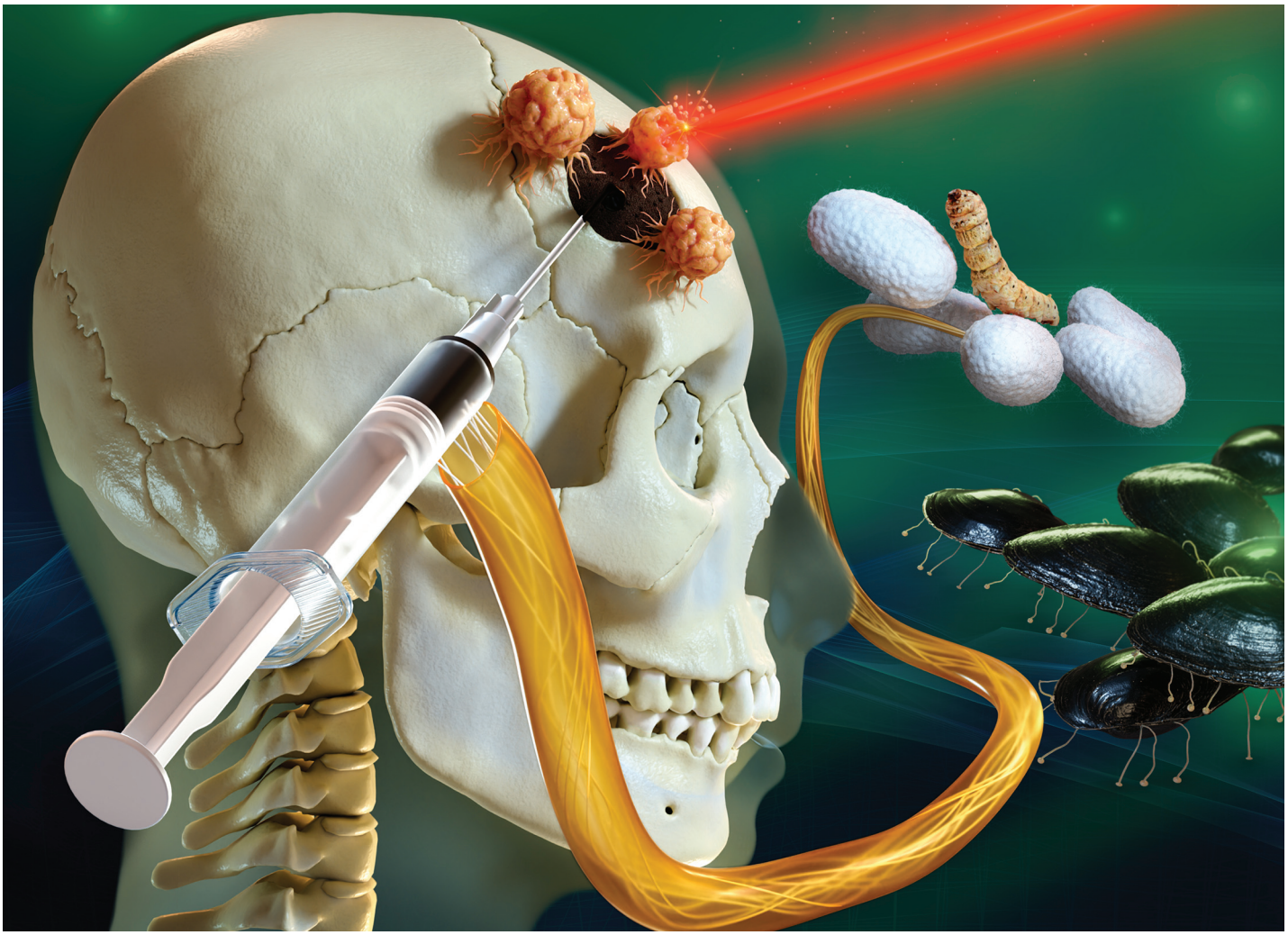

Showcasing research from PD. Dr Maleki's laboratory, University of Cologne Koeln, Nordrhein-Westfalen, Germany.

Theragenerative injectable bone-adhesive hydrogels for combined photothermal osteosarcoma therapy and bone repair

PD. Dr. Maleki and co-authors designed injectable self-healing and adhesive hybrid hydrogels from silk proteins, offering tissue adhesion, biocompatibility, and cancer therapy capabilities, providing a promising solution for osteosarcoma treatment and bone regeneration.

Image reproduced by permission of Hajar Maleki from *Biomater. Sci.*, 2025, **13**, 3544.

As featured in:

See Hajar Homa Maleki *et al.*, *Biomater. Sci.*, 2025, **13**, 3544.

ROYAL SOCIETY OF CHEMISTRY

rsc.li/biomaterials-science

Registered charity number: 207890

Biomaterials Science

ROYAL SOCIETY OF CHEMISTRY

PAPER

View Article Online
View Journal | View Issue

Cite this: *Biomater. Sci.*, 2025, **13**, 3544

Theragenerative injectable bone-adhesive hydrogels for combined photothermal osteosarcoma therapy and bone repair†

Shiyi Chen,[a] Nourhan Hassan,[b,c] Alexander Kopp,[d] Tatiane Eufrásio-da-Silva,[e] Jihene Arfaoui,[a,b,l] Benedetta Isella,[d,f] Ziyaad Aytuna,[a] Philipp Barnowski,[b,c,g,h] Gerhard Sengle,[b,c,g,h,i] Alireza Dolatshahi-Pirouz,[e] Nadja Kröger‡[j,k] and Hajar Homa Maleki *‡[a,b]

Injectable hydrogels with self-healing properties, tissue adhesion, biocompatibility, and cancer therapeutic capabilities offer a promising solution for addressing bone loss and residual tumor cells following surgical resection of osteosarcoma. In this study, injectable adhesive hybrid hydrogels were developed using natural silk-derived proteins, silk fibroin (SF), and silk sericin (SS). The sericin was surface functionalized with dopamine (DOPA) forming SSDOPA, while the silk fibroin was enzymatically oxidized (forming SFO) to introduce abundant catechol moieties on the polymer chains. These modifications enabled hydrogelation and self-assembly in the presence of copper ions (Cu^{2+}) and tannic acid (TA), creating an SFO-SSDopa-Cu^{2+}-TA hydrogel inspired by the mussel adhesion mechanism. The dynamic metal-catechol coordination bonds, along with other covalent and non-covalent interactions in the gel network, imparted excellent shear-thinning properties with 3D printability, injectability, self-healing (72.27 ± 9.35% after 6 cyclic), making it suitable for minimally invasive surgeries and targeted delivery applications. Additionally, the developed adhesive hydrogel demonstrated strong adhesiveness (664.03 ± 15.87 kPa and 854.15 ± 12.90 kPa on Gel- and Hap-based substrates respectively), showing excellent bonding performance to natural bone and tissue. Its black coloration enabled efficient absorption of near-infrared (NIR) light (reach 45–48 °C), facilitating the eradication of almost 60% osteosarcoma cells through photothermal therapy within 20 minutes of hydrogel irradiation with laser. Moreover, the developed SFO-SSDopa-Cu^{2+}-TA hydrogels promoted the proliferation and migration of pre-osteoblast cells, confirming their excellent biocompatibility. Coupled with good biodegradability, these hydrogels demonstrate significant potential as theragenerative materials for minimally invasive osteosarcoma treatment, providing a clinically translatable solution for repairing bone affected by the disease.

Received 12th April 2025,
Accepted 24th April 2025

DOI: 10.1039/d5bm00559k

rsc.li/biomaterials-science

[a]*Department of Chemistry, Institute of Inorganic and Materials Chemistry, University of Cologne, 50939 Cologne, Germany. E-mail: h.maleki@uni-koeln.de*
[b]*Center for Molecular Medicine Cologne, CMMC Research Center, Robert-Koch-Str. 21, 50931 Cologne, Germany*
[c]*Center for Biochemistry, Faculty of Medicine, University Hospital of Cologne, Joseph-Stelzmann-Street 52, 50931 Cologne, Germany*
[d]*Fibrothelium GmbH, Philipasstraße 8, 52068 Aachen, Germany*
[e]*Department of Health Technology, Technical University of Denmark, 2800, Kgs., Lyngby, Denmark*
[f]*Biomechanics Research Centre (BioMEC), School of Engineering, College of Science and Engineering, Institute for Health Discovery and Innovation, University of Galway, Galway, Ireland*
[g]*Department of Pediatrics and Adolescent Medicine, Faculty of Medicine and University Hospital Cologne, University of Cologne, Cologne, Germany*
[h]*Cologne Excellence Cluster on Cellular Stress Responses in Ageing-Associated Diseases (CECAD), University of Cologne, 50931 Cologne, Germany*
[i]*Cologne Center for Musculoskeletal Biomechanics (CCMB), 50931 Cologne, Germany*
[j]*Institute for Laboratory Animal Science and Experimental Surgery, University of Aachen Medical Center, Faculty of Medicine, RWTH-Aachen University, 52074 Aachen, Germany*
[k]*Department of Plastic, Aesthetic and Hand Surgery, St Antonius Hospital Eschweiler, 52249 Eschweiler, Germany*
[l]*Laboratoire de Chimie des Matériaux et Catalyse, Département de Chimie, Faculté des Sciences de Tunis, Campus Universitaire Farhat Hached d'El Manar, Université Tunis El Manar, 2092 Tunis, Tunisia*

† Electronic supplementary information (ESI) availableChemical and microstructure characterizations; preparation of commercial aqueous SF and SS solution; amino acid composition of SF and SS; different recipes of hydrogel adhesives SFO-SSDopa-Cu^{2+}-TA; evaluation of the adhesion on various common materials; sample preparation of adhesion tensile testing; producer of indirect assessment of cell viability; live/dead fluorescence staining assay for the attachment and proliferation; cell migration assay using culture inserts; NMR and IR spectra of SF and SFO after 1 day of oxidization; effect of different parameters (concentration of Cu^{2+}, volume ratio of SFO and SSDopa, TA%) on the gelation time; detachment force of hydrogel samples in adhesion tests; digital images from a thermal camera showing PTT efficacy of hydrogel samples with different ratios of SFO/SSDopa in air; PTT effect of hydrogel samples with different ratios of SFO/SSDopa at 0.75 W cm^{-2} power densities in PBS; dynamic monitoring images (0, 6, 12 and 24 h) of migration of MC3T3-E1 cell in different hydrogel components. See DOI: https://doi.org/10.1039/d5bm00559k

‡ Equally contributed authors.

1. Introduction

The skeletal system plays important roles in the human body, including bearing weight and protecting organs, while also facing multiple potential pathophysiological challenges. From a malignant bone tumor (osteosarcoma) which tends to happen in adolescents,[1,2] to degenerative orthopedic diseases caused by aging: fractures, osteoporosis, osteoarthritis, *etc.*, they run through the long line of life and impose huge economic burdens on individuals and society.[3] At present, autologous bone grafting is widely used in reconstructive orthopedic surgery because of its high mechanical properties, but the limited availability and donor site morbidity are problems that need to be overcome.[4,5] The development of bioactive materials provides new options for orthopedic diseases, which can serve as a substitute to assist in bone integration, repair, and even postoperative treatment of osteosarcoma.[3,6]

For bone bonding, Gluck put forward the idea of using biomaterials more than a century ago.[7] Diversified multifunctional hydrogel-based bioadhesives have been developed to this day, showing great potential in bone tissue engineering,[8–10] with biocompatibility and osteogenic potential effective for bone repair and reconstruction surgery.[7,11] For more aggressive diseases: osteosarcoma, traditional clinical treatment usually requires surgical resection combined with chemotherapy or radiation therapy.[1,12] These invasive treatment methods lead to significant bone loss, residual cancer cells, and tumor metastasis. Compared to these, photothermal therapy (PTT) is a non-invasive and efficient method in emerging cancer therapies. It is a safe therapeutic strategy that utilizes near-infrared (NIR) light responsiveness of photothermal agents (PTAs) to convert light into the local heat (>45 °C)[13] to thermally eradicate residual tumor cells locally and efficiently.[14] When increasing the enrichment of PTAs in tumor sites or endowing PTA with self-regulating photothermal conversion ability, selective killing of tumor cells can even be achieved.[15] Various PTAs with strong responses in the NIR region are used, such as metal (Au, Bi, Fe, Mo, among others),[12,16–18] MXene,[6] graphene oxide,[13] dopamine,[19] and some organic small molecules and dyes.[20] Building on this concept, our group has recently developed several 3D-printed silk fibroin (SF)-based composite aerogel scaffolds for applications in bone tissue engineering (BTE) and osteosarcoma treatment. By incorporating various PTAs—such as bismuth sulfide (Bi_2S_3) nanoparticles,[12] Ti_3C_2 MXene nanosheets,[6] and dopamine-modified electrospun bioactive glass nanofibers[5]—the resulting aerogels exhibit multifunctional properties, including photothermal anti-osteosarcoma activity and enhanced osteogenic potential.

SF is the main protein (70–80%) in natural silk derived from the silkworm,[21] *Bombyx mori*, and is now being investigated in a variety of biomedical applications.[22] The antiparallel β-sheet crystals formed by the hydrophobic repeating unit Gly-Ala-Gly-X in the SF chain[21,22] endow it with excellent mechanical properties, providing structural support for biomaterials (hydrogels, films, sponges and fibers),[23–25] along with assisting in antibacterial therapy[26] and promoting nerve regeneration.[27,28] Many studies have combined SF with other materials (such as PEG,[29,30] TA,[31,32] HA,[24] Ca^{2+},[33] *etc.*) to create adhesives suitable for tissue repair. However, there is still a lack of multifunctional bioadhesives based on SF for osseointegration and bone cancer treatment.

Compared to SF, the glue-like silk sericin (SS) as the second major silk protein (20–30 W%), has been less studied especially for biomedical applications, as for years it was believed to cause allergic reactions.[34] Such non-interactive use of these two silk-derived proteins continues to leading the disposal of large amounts of SS waste during the degumming process of silk fiber (50 000 tons of SS out of the 400 000 tons of dry cocoons produced globally), posing a hazard to the environment.[35] However, currently SS is gaining attention in the biomedical field as a soluble protein, and it has been found that SS is not only biocompatible but also has anti-inflammatory activity in cell culturing.[34] The abundant polar side chains (Ser, 30%; Asp, 20%) in the SS structure render it with higher hydrophilicity, better degradability, easier surface modification, and valuable antioxidant effects, as well as antimicrobial and anti-tyrosinase properties.[35–37] Recently, SS has been mixed with SF to fabricate biomaterials, such as 3D sponges, which not only complement both polymers' properties but also endowed the final material with improved properties compared to the pristine SF-based scaffolds.[34]

To advance the application of silk-based adhesive hydrogels for the minimally invasive treatment of bone tumors and to promote bone regeneration, we developed an injectable, self-healing hydrogel bioadhesive by combining two silk-derived proteins: silk fibroin (SF) and silk sericin (SS). The resulting hydrogel is designed for integration with bone tissue during minimally invasive surgery, offering strong bone adhesion and osteogenic potential, while simultaneously enabling local osteosarcoma ablation *via* photothermal therapy (PTT).

Inspired by the adhesive properties of mussel-derived catechol-containing amino acids, such as l-3,4-dihydroxyphenylalanine (DOPA),[38] extracted SF and SS were enzymatically oxidized or chemically functionalized with catechol moieties to yield oxidized SF (SFO) and catechol-modified SS (SSDopa), respectively. The incorporation of Cu^{2+} ions enabled the self-assembly in the biopolymeric solution through a dynamic metal–catecholate coordination, imparting shear-thinning and self-healing properties to the hydrogel network.[39] The addition of tannic acid (TA), a natural polyphenolic compound, to the protein solution introduced multiple cross-linking mechanisms—including Michael addition, hydrophobic interactions, and π–π stacking—in the resulting hydrogels, further enhancing their adhesive strength.[31,40] The injectability and adhesive performance of the hydrogel were optimized by fine-tuning the molar ratios of its components.

The resulting hydrogel was suitable for underwater applications, exhibiting strong adhesion to both bone and tissue. A series of chemical, biophysical characterization, and *in vitro* experiments have ascertained their surface modification, self-healing, adhesive properties, degradability, cytotoxicity, and

photothermal efficacy. The SFO-SSDopa-Cu^{2+}-TA-based hydrogel systems effectively enhance the adhesion properties of the SF-based aerogel scaffolds previously developed by our group. These innovative systems are anticipated to serve as a regenerative injectable and adhesive platform for precision minimally invasive surgical techniques. Their potential applications include bone regeneration and the treatment of osteosarcoma.

2. Materials and methods

2.1 Chemicals

All listed reagents and solvents were purchased from commercial suppliers and used without further purification. *B. mori* cocoons were purchased from a local farmer (Golestan Province, Iran). 1-Ethyl-3-[3-dimethylaminopropyl]carbodiimide (EDC, >98%), *N*-hydroxysuccinimide (NHS, ≥98%), tannic acid, sodium carbonate (Na_2CO_3, ≥99.5%), dopamine hydrochloride, tyrosinase from mushroom (≥1000 unit per mg), proteinase K from *Tritirachium album* (PK, ≥30 units per mg), gelatin from porcine skin (gel strength 300, type A), cell counting kit-8 (CCK8), osteoblast MC3T3-E1 cell line from mouse bone and osteosarcoma MG-63 cell line from human bone were obtained from Sigma-Aldrich-Chemie GmbH. Ethanol (EtOH, 99.9%), calcium chloride ($CaCl_2$, 99.99%), and copper sulfate ($CuSO_4$, 98.5–100.5%) were purchased from Thermo Fischer Scientific GmbH. Phosphate-buffered saline (PBS, pH 7.4 ± 0.2, after 1× dilution with DI water), Dulbecco's modified Eagle's medium (DMEM), fetal bovine serum (FBS), penicillin–streptomycin (P/S, 10 000 U mL^{-1}), trypsin-EDTA (0.05%) were purchased from Life Technologies GmbH. Calcein-AM (95%) and propidium iodide (PI, min. 94%) were purchased from Abcr Gute Chemie. The commercial SF and SS was provided by Fibrothelium GmbH.

2.2 Preparation of aqueous SF and SS solution

The SF and SS solutions were extracted from *B. mori* silkworm cocoons based on modified protocols reported by Zheng *et al.*[41] and Kumar *et al.*,[42] respectively (*cf.* Fig. 1a). Briefly, 5 g of silkworm cocoons were cut into coin-sized pieces and boiled in 2 L of Na_2CO_3 (0.02 M, 4.24 g) aqueous solution for 30 min. After degumming, the insoluble SF is taken out and washed before drying overnight. The dried SF (4 g) was dissolved in 20 mL of Ajisawa's reagent ($CaCl_2$/EtOH/H_2O, molar ratio of 1 : 2 : 8) in a beaker sealed with aluminum foil at 80 °C for 2 h. The dissolved SF solution was dialyzed to distilled water for 48 h using a 10 cm cellulose tube (3500 molecular weight cut-off, MWCO), with DI water changing every 2 h during day time to remove all impurities and salt. The obtained SF solution was centrifuged at 9000 rpm for 30 min, followed by diluting to a concentration of 4% (w/v) with DI water and maintained at 4 °C.

For the preparation of SS solution, the remaining 2 L of waste solution from the silk fibers degumming process was concentrated to 10 mL by boiling or evaporation under decreased pressure. Afterward, 10 mL of as-extracted SS solution was transferred to a dialysis bag (3500 molecular weight) cut-off, MWCO and dialyzed with DI water for 48 h, changing the water every 2 h during daytime. The purified SS solution was centrifuged at 9000 rpm for 15 min and dried into powder, being stored at room temperature for further characterization.

Commercially available SF and SS solutions (Fibrothelium GmbH, Aachen, Germany) were used as a standard for the comparison of the extracted proteins. The extracted progress from Fibrothelium GmbH is described in ESI.†

2.3 Surface modification of SF and SS polymers

To bring catechol groups into the system, SF and SS underwent surface modification (*cf.* Fig. 1b). For SF, catechol groups can be easily obtained through oxidation by the tyrosinase enzyme.[6] The SF solution (4%) and tyrosinase enzyme (1000 U mL^{-1}) were mixed gently in a 25 : 1 volume ratio and placed in the oven at 40 °C overnight. The resulting solution SFO containing catechol-modified side chains showed a change in color toward light orange, which can be determined by UV-Vis spectroscopy. For SS, some amide bond in the chain were broken after concentration progress in lab due to harsh conditions, the commercial SS powder (Fibrothelium GmbH, Aachen, Germany) was used for surface modification. Here, the EDC/NHS reaction was used to activate the carboxyl groups –COOH on the SS chain and react them with the amine groups $–NH_2$ on the dopamine monomers through the formation of amide bonds, introducing catechol groups. This process was based on a simply modified procedure reported previously by Yan *et al.*[43] In short, 0.5 g of SS powder extracted from cocoons was dissolved in 10 mL of DI water and adjusted to pH 6 with hydrochloric acid (HCl, 5 M). Afterward, 2.5 mM of EDC (0.004 g) and 12 mM of NHS (0.014 g) were added to the SS solution and reacted in an ice bath under a dark environment for 30 min to activate the carboxyl groups on the SS chain. Accompanied by the addition of excessive dopamine (74 mM, 1.4 g) monomer, the reaction continued for 1 h. The obtained SSDopa solution was dialyzed against DI water in a cellulose bag (3500 molecular weight cut-off, MWCO) for 3 days until excess EDC, NHS, and dopamine monomers were removed. The DI water was changed every 2 h during the daytime. The resulting solution was centrifuged at 9000 rpm for 15 min to obtain the supernatant of pure SSDopa with a concentration of around 2% (w/v). The obtained SFO and SSDopa solutions were stored at 4 °C for the future preparation of the adhesive hydrogel.

2.4 Synthesis of injectable adhesive hydrogel systems

The SFO-SSDopa-Cu^{2+}-TA hydrogel adhesive was prepared by mixing a certain proportion of SFO (4%), SSDopa (2%), Cu^{2+} (0.5 M) solution obtained by dissolving copper sulfate (Cu_2SO_4) in DI water, and with different percentage of tannic acid (TA) (*cf.* Fig. 1c). For example, for the formulation of 4 (*cf.* Table S2†), after mixing 2.18% of SF solution (4%, 1 mL) with 0.32% of SSDopa solution (2%, 0.3 mL) at room temperature, 0.008 mol L^{-1} of Cu^{2+} solution (0.5 M, 30 μL) was added for

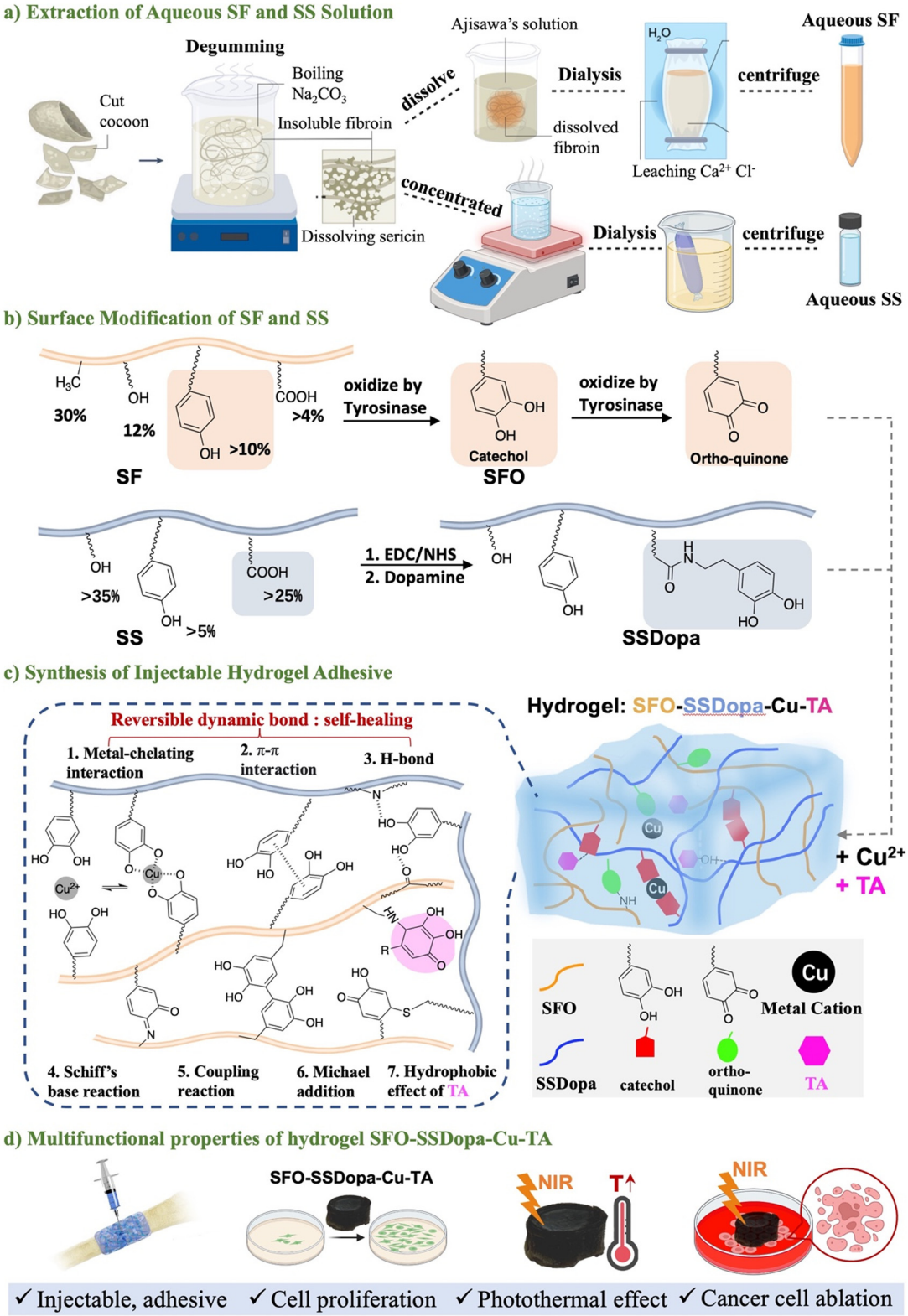

Fig. 1 (a) Schematic diagram of the extraction process of silk fibroin (SF) and silk sericin (SS) aqueous solutions. (b) Different strategies for surface modification of catechol groups onto SF and SS chains. The percentage of functional groups on the main chain is calculated based on the amino acid composition (*cf.* Table S1†) in the literature.[22,36] (c) Schematic illustrating the preparation procedure of SFO-SSDopa-Cu^{2+}-TA-based hydrogel systems with different crosslinking methods in networks. (d) Multifunctional properties of injectable adhesive hydrogel SFO-SSDopa-Cu^{2+}-TA, including bone binding, the proliferation of preosteoclasts, photothermal effect, and osteosarcoma cell ablation.

metal-chelating crosslinking method. We adjusted the pH of the mixed solution to 11 with KOH solution (1.5 M, 35 μL), followed by the addition of 0.27% TA solution (1%, 0.5 mL) slowly, to obtain the final hydrogel pre-solution with a pH of about 9. The pre-solution was taken in a syringe to conduct gelation and aging in an oven at 60 °C for 3 days. In order to obtain injectable hydrogel with adhesive properties, different formulations were synthesized and listed in Table S2.†

2.5 Injectability, self-healing, rheological and compressive mechanical properties

The hydrogel synthesized in syringes was hand-pressurized to facilitate the visual extruding testing. Then the extruded shapes were submerged in water for 10 minutes to observe their stability in wet environment or underwater stability. Then the hydrogel in the syringe was also loaded onto a micro-extrusion 3D printer (Hyrel 3D, Engine SR, with a resolution of 5 μm in (x, y) directions and 1 μm in the z direction) and printed into scaffolds to test their printability of complex into fine structures. Prior to 3D printing, we evaluated the rheological behavior of adhesive hydrogels using Discovery Hybrid Rheometer HR-2 (TA Instruments) using 8 mm parallel plate geometry with a gap distance of 1000 μm. The viscosity properties (G4, n = 4) were investigated at 25 °C and 37 °C. Thus, it was investigated the oscillation strain sweep (OS) at angular frequency of constant 1 Hz (6.28318 rad s^{-1}) and oscillation strain up to 1000%. Moreover, rheological self-recovery (SR) test was performed by changing strain from 1% up to 300% with 300 s of recovery between cycles. For both OS and SR, the samples were reconstituted and cured for 80 min at 60 °C, and the analyses performed at 25 °C.

Furthermore, we also explored compression mechanical tests (G4, n = 5), which they were performed by using an Instron instrument (model 5967 – U.K., 50 N load cell) at the speed rate of 0.5 mm min^{-1}. Also, a digital caliper to acquire the specimens' dimensions. The 100 μL of the samples were reconstituted in a 4.7 mm diameter mold and cured for 3 hours min at 60 °C. Afterwards, the samples were immersed in PBS at 37 °C for 15 minutes, prior the tests. The compressive young modulus was computed as the slope of the stress–strain curve, considering 15–25% strain region, while the toughness from the area under the curve. The compressive stress at 40%, the breaking points and compressive ultimate stress were also in processed.

2.6 Adhesion test

The hydrogels were applied to chicken bones and substrates-coated metal sheets for the evaluation of their adhesion properties on different tissues (n = 3). For bone adhesion, an *ex vivo* test using chicken bones was cut into two pieces and then adhered with 50 μL of hydrogel, placed in a wet environment (surrounded by wet cotton) in the oven at 37 °C for 3 h. Hydrogel was also injected into the bone to seal the perforated penetrating defects and placed in an oven for 3 h in the same environment. Afterward, a water bottle was rinsed against the blockage to observe whether the hydrogel would be dislodged. For tissue adhesion, an adhesion test was performed based on the ASTM F2255-05 standard using a machine of Zwick-Roell Z010. 20% gelatin in PBS was used as a substrate to simulate tissues, and 14% hydroxyapatite (Hap)/6% gelatin was used to simulate bones as bones contain 70% HAp.[44] They were coated on the end of metal slides (50 mm × 10 mm × 1 mm) with a coating area of 15 mm × 10 mm. The layers were placed opposite each other and 50 μL of adhesive hydrogel was injected in the middle and fixed together with an area of 10 mm × 10 mm (*cf.* Fig. 5c). The control experiments were two pieces of coated metal sheets connected (10 mm × 10 mm) without hydrogel samples in a sandwich. After that, a weight (50 g) was pressed on the joints and placed in an oven at 37 °C in a humid environment (*cf.* Fig. S2†). They were removed from the oven after 3 h and cooled down. The lap shear adhesion strength of incubated samples was tested at a constant speed of 5 mm min^{-1} to obtain the adhesive strength. The adhesion performance is analyzed through detachment force $F[N]$, work of adhesion W [mJ], and adhesion strength [kPa]. The detachment force is the maximum point of the pull-out load–displacement curve, and the adhesion work is the area under curves. The adhesion strength was calculated as the ratio between the maximum force detected during the test and the contact area.

2.7 *In vitro* photothermal property

To investigate the photothermal properties of adhesive hydrogels, hydrogels (formulation 0, 1, 4, 8, 9 at a cylindrical shape with a diameter and height of 5 mm) were placed in a small volume of PBS (1 mL) as testing in a wet environment. The corresponding dried aerogel of the same size was tested directly in a dry environment (in air). The aerogel and hydrogel of SFO-SSDopa-Cu^{2+}-TA (formulation 4 in Table S2†) were subjected to 808 nm NIR laser irradiation at different power densities for 500 s (0.40, 0.45, and 0.50 W cm^{-2} in the air; 0.50, 0.75, and 1.0 W cm^{-2} in PBS) to find the appropriate power for different environments. These proper power (0.45 W cm^{-2} in the air; 0.75 W cm^{-2} in PBS) were then used to test different aerogel and hydrogel samples (recipe 0, 1, 8, and 9 in Table S2†) in the relative environment. The temperature change of the hydrogels was recorded by a thermal camera (Voltcraft WB-300, Germany) taking pictures every 20 seconds. Finally, an SFO-SSDopa-Cu^{2+}-TA (formulation 4 in Table S2†) aerogel was subjected to an "on–off" cycling test to check the photothermal stability of the materials. The aerogel was irradiated with a 0.45 W cm^{-2} power density in the air (laser on for 3 min), then cooled naturally to room temperature (laser off for 2 min). Such a cycle was repeated for four rounds without interruption. Similar experiments were conducted on bones. The representative gel (formulation 4 in Table S2†) was applied to chicken bones and continuously irradiated at 0.6 and 0.8 W cm^{-2}. Subsequently, a cyclic test (laser on: 1 min; off: 1 min) was conducted at 0.6 W cm^{-2} for testing the photothermal stability.

2.8 *In vitro* photothermal ablation of bone cancer cells

Osteosarcoma MG63 cell line was used to evaluate the *in vitro* PTT performance of hydrogel SFO-SSDopa-Cu^{2+}-TA for cancer cell ablation under NIR-laser exposure. Approximately 7.5×10^4 cancer cells were seeded per well into a 24-well plate. After 24 hours, the hydrogel SFO-SSDopa-Cu^{2+}-TA was cut into 1 mm thick discs with a similar diameter to the plate and placed into the wells. The cells were treated by PTT with NIR laser (808 nm, 0.75 W cm^{-2}) for 0, 5, and 20 min, respectively. The hydrogel and medium were discarded, and cells were gently washed with PBS. The cell viability was measured by CCK-8 assay ($n = 3$).

2.9 *In vitro* biodegradation performance

The hydrogels (formulations 1, 4, 8, and 9) were supercritically dried to obtain corresponding aerogels, which were divided into similar weights, and the initial weight (W_0) of each sample was recorded. The samples were placed in a 24-well plate and immersed in two different degradation media groups (1 mL per well): phosphate-buffered saline (PBS) and proteinase K (PK) solution (0.5 U mL^{-1} in PBS). Incubation was carried out in a 37 °C shaking water bath for up to 21 days, with the degradation medium changed every 2 days. The old degradation solutions containing a very small number of samples were collected and kept in a refrigerator at −20 °C. At specific time intervals (7, 14, and 21 days), the remaining samples were removed from the liquid environment and combined with the solid fraction obtained from the collected degradation medium after centrifugation. The weight (W_t) was measured after drying. The decrease in sample weight is represented by W_d (where, $W_d = W_0 - W_t$), and the overall degradation of the sample can be expressed by eqn (1).

$$\text{Total °. of sample}\,(\%) = \frac{W_d}{W_0} \times 100\%, \quad (1)$$

2.10 *In vitro* biocompatibility evaluation

All hydrogels used for cellular experiments were sterilized by irradiation under UV for 30 min after a gradient of ethanol washing (ethanol/H_2O: 100%, 70%, 50%, 30%), and then rinsed once more with sterile PBS. In the indirect assessment (*cf.* Fig. S3†), 20 mg mL^{-1} of different hydrogels were soaked in complete culture medium DMEM (10% FBS, 1% P/S) for 1, 3, 5, and 7 days to obtain conditional mediums. The fresh culture medium was incubated for up to 7 days at 37 °C and served as a control medium to the specific time point. MC3T3-E1 cells were seeded in 96-well plates (1×10^4 per well) along with a complete culture medium. After 24 hours, the medium was replaced with a conditioned medium. After another 24 h incubation, the medium was removed, and 10% CCK-8 reagent was added to each well (100 μL) followed by 4 h incubation. The cell viability was determined by reading its optical density (O.D.) value at 450 nm by a *TECAN* ELISA reader. Furthermore, higher concentrations (100 mg mL^{-1}, soaking for 7 days) of conditional media were tested. Cells were seeded at 7×10^4 per well in 24-well plates, and after 24 h, the medium was replaced with a conditional medium continuing the culture. Cell proliferation was determined by CCK-8 assay after culturing another 24 h and 72 h, respectively.

2.11. Pre-osteoblast cell attachment and proliferation

The attachment and proliferation of MC3T3-E1 cells on different hydrogels were assessed by direct cell culture (*cf.* Fig. S4a†). The hydrogel was cut into 1 mm thick discs with a similar diameter to the bottom of the well plate and treated in a complete culture medium for 24 h. Afterwards, the old medium was discarded and the medium containing cells (500 μL, 7.5×10^4 cells per well) was slowly added onto the hydrogel surface directly. Live/dead fluorescence staining assay was carried out at each time point after 1, 3, and 5 days of incubation. The staining solution was a PBS solution (2 mL) containing calcein-AM (5 μL) for live cells and propidium iodide (PI, 6 μL) for dead cells. After aspirating the medium from the well plates, 200 μL of staining solution was added to each well and imaged with a fluorescence microscope (Olympus IX83) after incubating in the dark for 20 min. Live cells were excited under blue light ($\lambda_{excitation}$ = 490 nm) and photographed under green fluorescence ($\lambda_{emission}$ = 515 nm), while dead cells were excited under green light ($\lambda_{excitation}$ = 535 nm) and photographed under red fluorescence ($\lambda_{emission}$ = 617 nm).

2.12 Co-culture system of hydrogel and cells

The 3D cell culture system preserves interactions between cells and extracellular matrix (ECM), such as hydrogel, in multiple dimensions.[45] Briefly, 200 μL of hydrogel precursor solution was gently mixed with cell medium (50 μL containing 1.5×10^5 cells per well) in a 24-well plate and then gelated in an incubator together. 500 μL of complete culture medium was added at the first moment after gel solidification. After 24 h of incubation, a CCK8 assay was performed to determine cell viability (*cf.* Fig. S4c†).

2.13 *In vitro* cell migration

To determine the migratory capacity of MC3T3-E1 osteoblastic cells in hydrogel conditional media (20 mg mL^{-1}, collected after 5 days), ibidi culture-insert 2-well was used to culture the cells (*cf.* Fig. S5†). Cells in normal medium (500 μL, 5×10^5 cells) were seeded into culture inserts and allowed to attach. After 24 hours, the culture insert was carefully removed with sterile tweezers, creating a physical gap within a cell monolayer. The cells were washed gently with PBS to remove debris and unattached cells, followed by adding conditional media. The time point when the conditional culture medium was added, was set as 0 h and within the next 24 h. The process of cell migration into the gaps was monitored by taking photos every hour using a *Leica* microscope.

2.134 Circular dichroism spectroscopy

SF, SFO, SS, and SSDopa were each dialyzed into Millipore water at a concentration of 200 μg ml^{-1}. Ellipticity θ (in mdeg) were recorded using a Jasco J-715 spectropolarimeter with a

1 mm path length quartz cell (Hellma, Germany), covering the range from 260 to 170 nm at 20 °C. Millipore water was used as blank.

3. Results and discussion

3.1 Fabrication, chemical, and microstructural characterization

Targeting the development of injectable adhesive hydrogel considering the precursor sources from two main silk-derived proteins: the aqueous solution of silk SF and SS were first extracted from the silkworm cocoon, as confirmed by the ^{1}H NMR spectra (*cf.* Fig. 2a). Noteworthily, both SF and SS chains are composed of multiple amino acids through amide bonds, some of which are of the same type with similar characteristic peaks. For example, the signal of the aromatic side chains of the tyrosine (Tyr) is at 6.8–7.08 ppm (d). For serine (Ser) α, Tyr α, alanine (Ala) α, glycine (Gly) α, and Ser β, the signals are located between 3.9–4.57 ppm (g, b, h, e, f, respectively). The amino acid sequence signal of Tyr β is at 3.04 ppm (c). The signal at 1.21 ppm (i) can be assigned to Ala β. The spectrum of SS has more signals, as the peak at 3.2 ppm (a) is the accumulation of the –CH_2– methylene group on lysin (Lys). The signal at 2.7 ppm is contributed by the aspartic acid (Asp) β because the content of Asp in SS is as high as 20%, while Asp in SF is only 4% which is not shown in the spectrum. The small signals at 1.5–2.4 ppm are composed of β-CH_2 methylene group from glutamine (Gln), glutamic acid (Glu), and isoleucine (Ile), among others which is consistent with the literature.[6,12,46–48]

In addition, the functional groups and molecular conformations of lab-extracted SF and SS were compared with commercially available products from Fibrothelium GmbH, Germany through FTIR analysis (*cf.* Fig. 2b), to ensure that the lab-extracted silk proteins are usable and effective. The characteristic peaks in IR spectra of extracted SF and SS were almost identical to those commercially available products and consistent with previous reports[58,59] – by showing similar absorption peaks of amide I (SF: 1619 cm^{-1}; SS: 1643 cm^{-1}), which are made up of 70–85% C═O stretching vibration. The characteristic vibration ranged in 1470–1570 cm^{-1} (SF: 1513 cm^{-1}; SS: 1517 cm^{-1}) is caused by amide II (secondary N–H bending). When the amide II forms change from random coils to β-sheet, the combination of C–N stretching and N–H plane bending leads to the amide III (SF: 1229 cm^{-1}; SS: 1243 cm^{-1}).[35] The significant difference between the IR spectra of SF and SS is that in the amide A region, the amide A band of SS (3269 cm^{-1}) is wider than that of SF (3277.02 cm^{-1}). This is because SS has more random curls, while SF has higher crystallinity.[36] The secondary structures of SF, SS, and their catechol-modified derivatives, SFO and SSDopa, were characterized by circular dichroism (CD) spectroscopy. The CD spectra of SF and SFO exhibited strong nega-

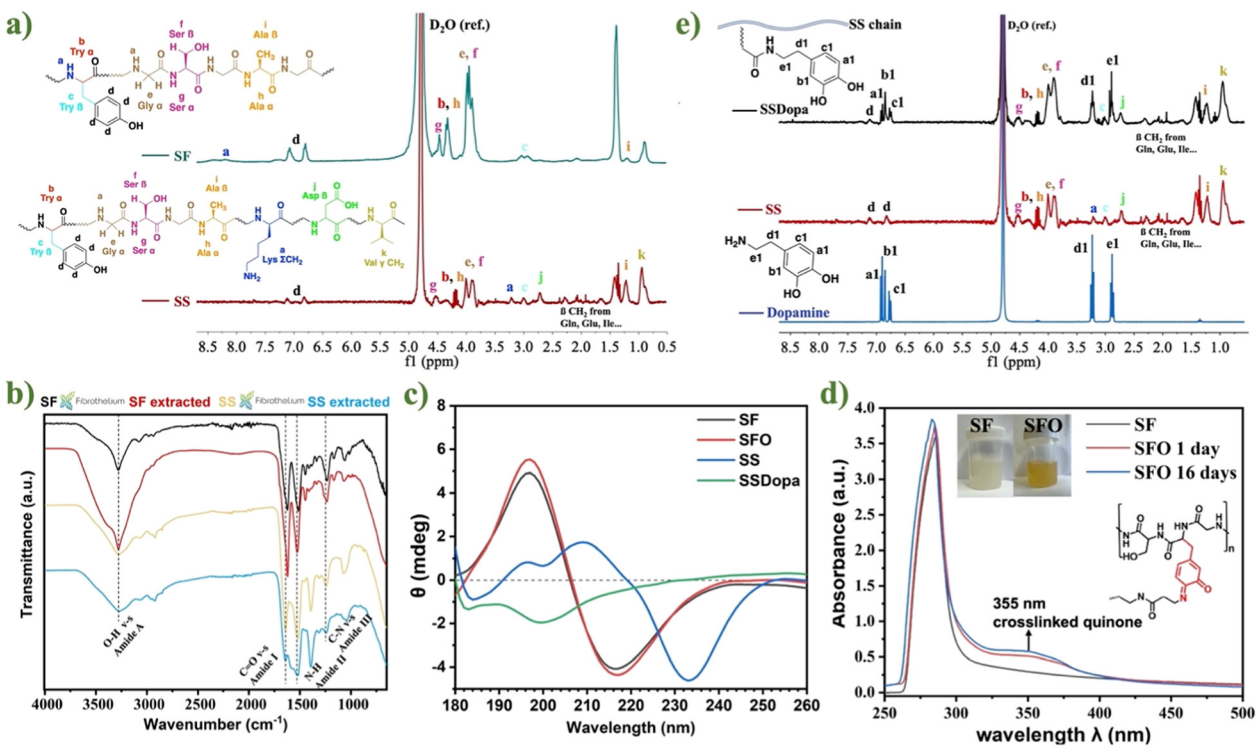

Fig. 2 (a) ^{1}H NMR spectra of extracted SF (green) and SS (red). (b) FTIR spectra of extracted SF and SS, compared with commercially available products. (c) CD spectra of extracted SF, SS and modified SFO, SSDopa at 0.2 μg ml^{-1}. (d) UV-Vis spectra of SF and oxidized SFO after 1 day and 16 days. (e) ^{1}H-NMR spectra of SSDopa, unsubstituted SS, and dopamine monomer.

tive bands at 218 nm, characteristic of β-sheet structures (*cf.* Fig. 2c). Oxidation of SF to SFO did not lead to significant changes in the spectra, as the oxidation only occurs at the phenol moieties of tyrosine residues and does not affect the formation of hydrophobic domains responsible for β-sheet assembly. In contrast, the CD spectrum of SS showed a negative peak at 234 nm, indicative of α-helical structures. After the introduction of dopamine groups, the α-helix structure of SS was disrupted in SSDopa, leading to a random coil conformation, as evidenced by the appearance of a negative band around 198 nm.

After SF and SS were successfully extracted, they were either oxidized or surface functionalized to introduce catechol groups into the structure, preparing for mussel adhesion strategy and metal chelating to form a self-assembled adhesive hydrogel. The high content of tyrosine groups in the SF chain was oxidized to SFO by the tyrosinase enzyme, generating target catechol groups and some reactive *ortho*-quinone. The successful change from SF to SFO was proven by UV-Vis spectroscopy (*cf.* Fig. 2d), where the UV-Vis spectra of SF and SFO (1 and 16 days after oxidation, respectively) presented strong absorption peaks at 280 nm (due to $\pi \rightarrow \pi^*$ electronic transitions of aromatic amino acid residues on the protein chain).[49] In the oxidized SFO, there is an additional peak at 355 nm with the solution color changing to bright orange. This is from the cross-linked product formed between *ortho*-quinone and amino groups exhibiting absorption at 350 nm.[50] Compared with SFO after 16 days of oxidation and 1 day, the absorption intensity at 355 nm is slightly increased, indicating that more catechol groups oxidized into orthoquinones with the extension of time. Additionally, compared with pure SF, the FT-IR spectra of SFO (*cf.* Fig. S6b†) produced new peaks at 1280 and 1250 nm which are assigned to the C–O vibration bands for catechol.[51]

Next, in order to introduce catechol groups into SS, SSDopa was synthesized through the classic EDC/NHS coupling reaction to conjugate dopamine molecules onto the SS backbone. The successful modification of SS to SSDopa was confirmed by ^{1}H NMR spectra (*cf.* Fig. 2e). The characteristic peaks of dopamine at 6.7–7 ppm are attributed to the primary amine group and the hydrogens on the benzene ring of the catechol group, respectively. The peaks at 3.2 ppm and 2.8 ppm are assigned to the methylene groups on the alkyl chain. The same relevant peaks appeared in the modified SSDopa spectrum, only shifted from 6.7–7 ppm to 6.5–6.8 ppm due to the influence of the carbonyl group on the amide bond. At the same time, there was no peak associated with polydopamine.

After obtaining the catechol-modified SFO and SSDopa precursor solutions, they were mixed based on different formulations (*cf.* Table S2†), followed by gelation and aging at pH 9 and 60 °C for 3 days. It was found that the hydrogel solution containing only SFO reached the gelation point after 8 days (*cf.* Fig. 3a). Whereas when SSDopa was added into the system, the gelation time was greatly reduced to 1 day, proving that the catechol groups present in abundance in SSDopa can help form a hydrogel network through chemical crosslinking. When the copper (Cu^{2+}) ions were added to SFO-SSDopa, the gelation time was slightly reduced by 4 hours. This proves the contribution of the metal-catechol self-assembling strategy in the hydrogel network; nevertheless, the time reduction was less compared to chemical crosslinking. Furthermore, the addition of TA to SFO-SSDopa led to SFO-SSDopa-TA, which undertook around only 3 h to form a gel indicating that the large number of phenolic hydroxyl groups in the TA structure participated in the formation of the network. Ultimately, the hydrogel solution SFO-SSDopa-Cu^{2+}-TA containing both Cu^{2+} and TA was capable of gelating after only 90 min. Therefore, in such a hydrogel network, there are both metal chelating crosslinking based on catechol-copper ions interaction, as well as chemical crosslinking brought by catechol and *o*-quinone groups. In SFO-SSDopa-Cu^{2+}-TA, to control the gelation kinetics, and hydrogel key properties like self-healing and adhesiveness, three synthetic parameters were controlled (*cf.* Fig. S7†): (1) the concentration of Cu^{2+}, (2) volume ratio of SFO and SSDopa, (3) weight/volume ratio of TA in the network. After excluding phase separation and gum formation, a representative hydrogel adhesive SFO-SSDopa-Cu^{2+}-0.008-TA0.27 (formulation 4) was determined for all biological tests.

The prepared hydrogel with different formulations (SFO-SSDopa, SFO-SSDopa-Cu^{2+}, SFO-SSDopa-TA, SFO-SSDopa-Cu^{2+}-TA) underwent unidirectional freeze casting to generate open macroporosity for cell infiltration followed by supercritical CO_2 drying method to obtain corresponding aerogels with subtle differences in IR spectra (*cf.* Fig. 3b). All aerogels show similar characteristic peaks in the amide I, II, and III regions (1622 cm^{-1}, 1526 cm^{-1}, and 1233 cm^{-1}, respectively). However, samples containing Cu^{2+} have an additional peak at 1071 cm^{-1}, which is due to the chelation between the hydroxyl group of catechol and metal ions through coordination.[52] The peak of the samples containing TA shows a certain enhancement at 1320 cm^{-1}, possibly due to the introduction of more phenolic hydroxyl groups in the TA structure, resulting in more significant bending vibrations of the –OH group.

The microstructure of hydrogel adhesive was studied by scanning electron microscopy (SEM). The hydrogel was unidirectionally freeze-cast before supercritical drying. The unidirectional growth of ice crystals during the freeze casting in the hydrogel and the subsequent removal of growing ice by sublimation make the final samples display different morphologies on the transverse and longitudinal sections. In the SEM micrographs of SFO-SSDopa and SFO-SSDopa-Cu^{2+}-TA (*cf.* Fig. 3c), layered porous structures can be found in transverse sections of the hydrogels. The longitudinal section tends to be more inclined towards a complete flake-like structure, which forms the transverse porous morphology. This is consistent with the expected results of unidirectional freeze-casting progress. Furthermore, comparing the transverse sections images of SFO-SSDopa and SFO-SSDopa-Cu^{2+}-TA, it was found that the flaky shape of SFO-SSDopa-Cu^{2+}-TA was not as complete as that of SFO-SSDopa. This may be because, in the structure of SFO-SSDopa hydrogel, the β-sheet caused by hydrogen bonds has made a great contribution, while in SFO-SSDopa-Cu^{2+}-TA,

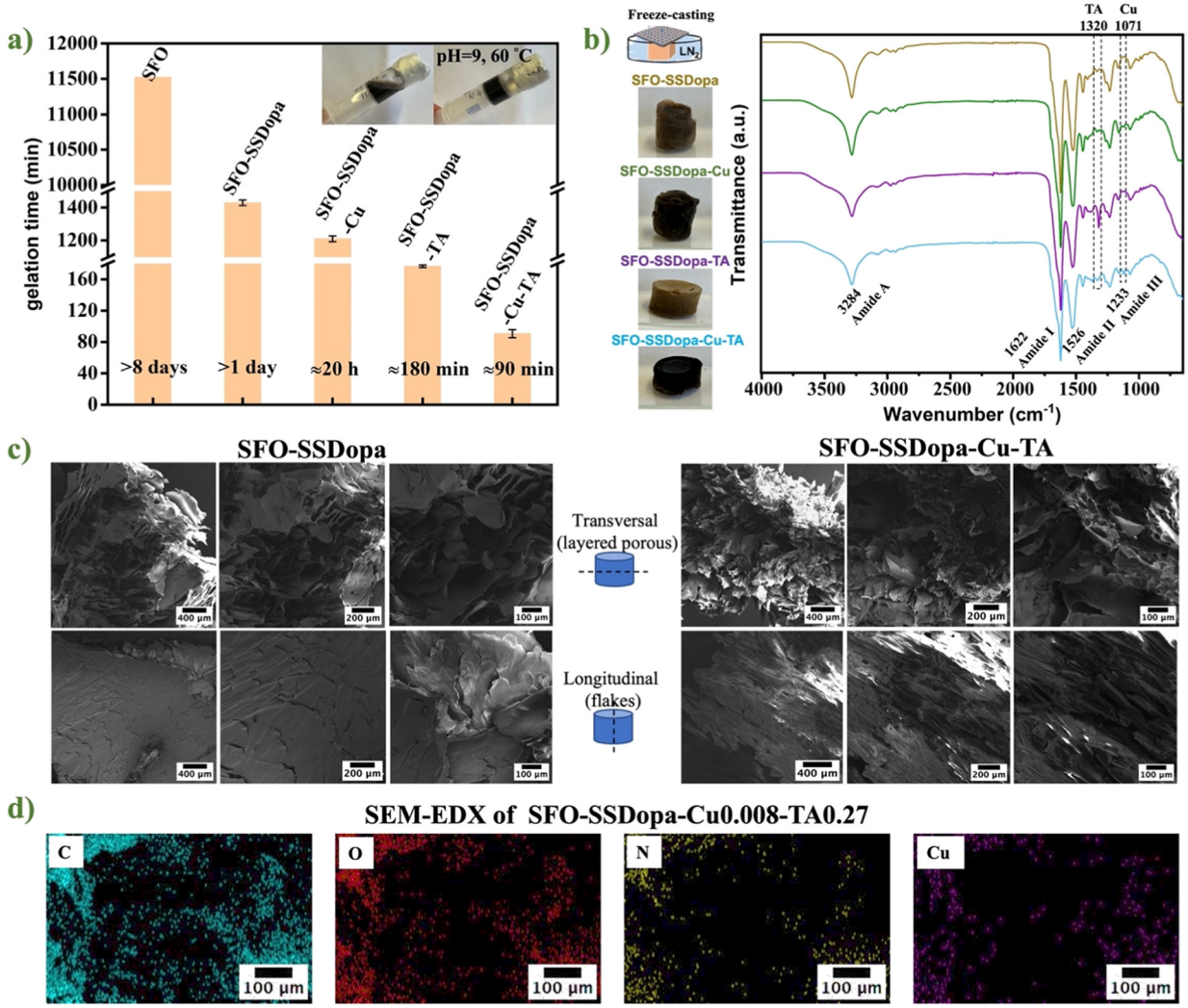

Fig. 3 (a) Gelation time of hydrogel adhesive with different compositions at pH 9 and 60 °C. *n* = 6 replicates. (b) Digital camera images and IR spectra of aerogels obtained after freeze-casting and supercritical drying of hydrogel adhesive SFO-SSDopa (brown), SFO-SSDopa-Cu^{2+}- (green), SFO-SSDopa-TA (purple) and SFO-SSDopa-Cu^{2+}-TA (blue). (c) SEM micrographs of aerogels obtained after freeze-casting and supercritical drying of hydrogel SFO-SSDopa and SFO-SSDopa-Cu^{2+}-TA with different magnifications. Sections of aerogel were cut from the transverse and longitudinal directions. (d) SEM-EDX images of corresponding aerogel from the representative hydrogel adhesive SFO-SSDopa-Cu^{2+}-0.008-TA0.27 with elemental analysis of C, N, O, Cu.

the Cu^{2+} for metal chelating and additional TA macromolecules have broken the folding, making the microstructure more complex. SEM energy dispersive X-ray spectroscopy (SEM-EDX) in conjunction with SEM helped to prove the successful incorporation of metal cations Cu^{2+} in the hydrogel network (*cf.* Fig. 3d). The content of carbon (C, 59.6%), nitrogen (N, 18.9%), oxygen (O, 19.5%), copper (Cu, 0.3%), and other important elements in the hydrogel were found through the elemental mapping with homogeneous distribution in the gel network.

3.2 Injectability, self-healing, rheological and compressive mechanical properties

In order to be used in minimally invasive surgery, the developed hydrogel adhesive must have certain injectability and self-healing properties. The hydrogel adhesive SFO-SSDopa-Cu^{2+}-TA was loaded in the syringe and extruded by hand (*cf.* Fig. 4a) and afterward through 3D printing (*cf.* Fig. 4b). After 3D printing from a computer aided design (CAD) model, macropores (1000 μm) can be observed in the multilayer scaffold as expected. These hydrogels can be used for designing scaffolds with more fine structures or minimally invasive surgery. Besides that, the hydrogel can restore its overall shape after extrusion, when the hydrogel was cut and its pieces put close together, the boundary between the gel pieces became fuzzy after a few seconds (*cf.* Fig. 4c). After continuous testing, it was found that most samples can be quickly self-healed within 20 s, contributed by plenty of reversible dynamic bonds.

The viscosity test (*cf.* Fig. 4d and e) performed for SFO-SSDopa-Cu^{2+}-TA showed shear thickening behavior before

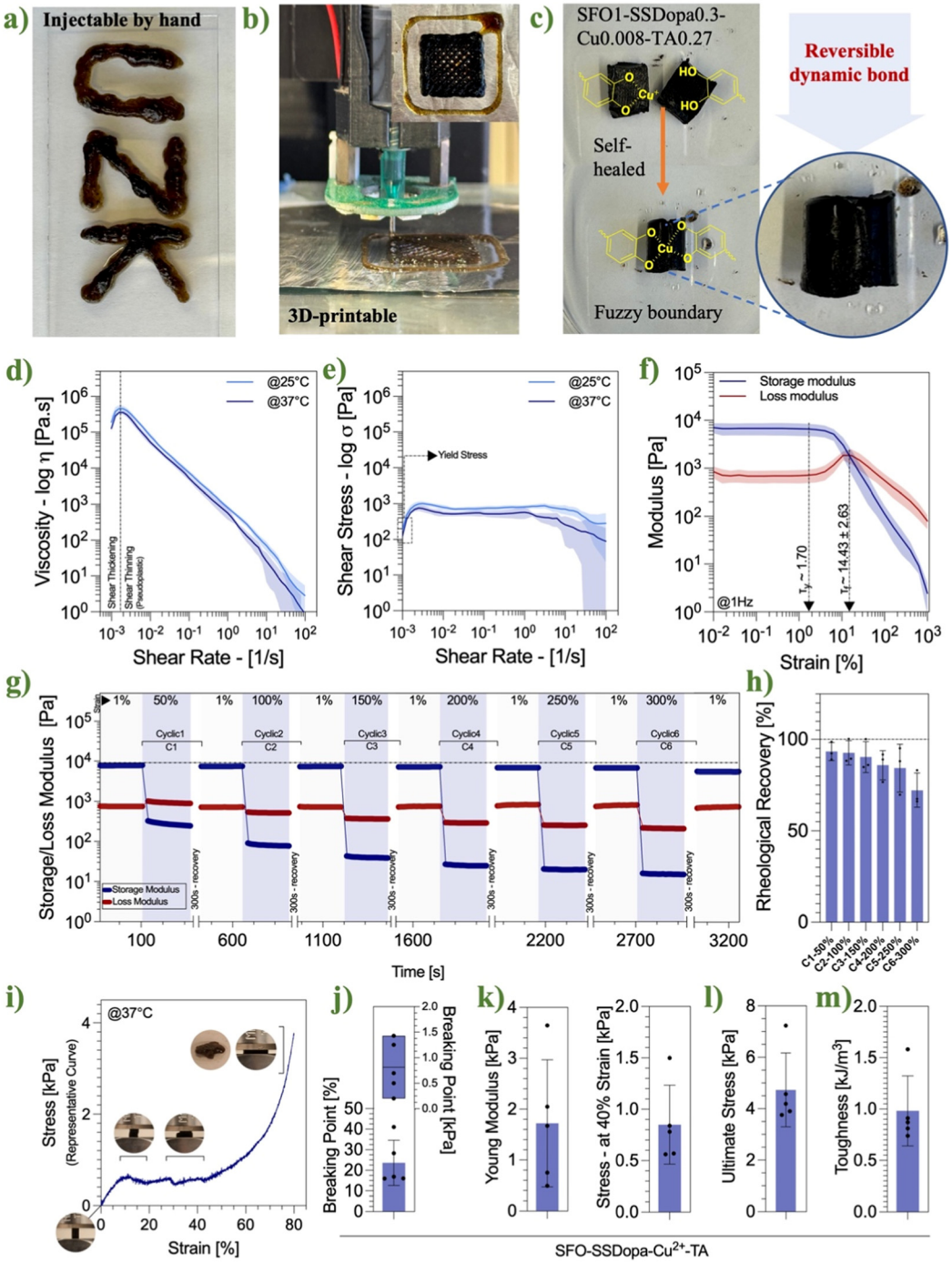

Fig. 4 (a) The digital camera images of hydrogel adhesive SFO-SSDopa-Cu^{2+}-TA with writability and (b) 3D-printability for fine structure. (c) Digital camera images of self-healed bulk hydrogel after cutting. (d) Viscosity and (e) shear stress of hydrogel adhesive SFO-SSDopa-Cu^{2+}-TA. (f) Strain amplitude sweeps of hydrogel adhesive SFO-SSDopa-Cu^{2+}-TA with storage modulus *G′* (blue) and loss modulus *G″* (red). (g) Continuous step-strain measurements of hydrogel SFO-SSDopa-Cu^{2+}-TA with high strain (50–300% in six cycle) and low strain (1%) to characterize the self-healing properties with 300 s of recovery between cyclic. (h) Rheological recovery of six cyclic testing. (i) Representative curve of compressive mechanical test, (j) breaking point, (k) compressive young modulus, (l) ultimate stress and (m) toughness of hydrogel adhesive SFO-SSDopa-Cu^{2+}-TA.

0.002 s^{-1} of shear rate, afterwards showed thinning behavior from this range shear rate. The viscosity of both temperatures followed similar profiles up to ~15 s^{-1} shear rate, then the hydrogel at 37 °C showed a drop in the viscosity with the shear rate increases; being confirmed from shear stress *versus* shear rate curve which presented similar behavior. Moreover, the yield stress for the hydrogel at 25 °C presented 189.03 ± 90.61 Pa, while at 37 °C presented 126.14 ± 6.57 Pa.

The critical strain and self-healing ability of hydrogels were explored more data-driven, through their storage modulus G' and loss modulus G''. The rheological tests of the strain amplitude sweep mode and continuous step strain measurements were carried out. Mechanical rheological analysis of hydrogel SFO-SSDopa-Cu^{2+}-TA showed that at 1 Hz the storage modulus was around 7025 ± 1709 Pa and loss modulus of 849 ± 240 Pa during amplitude frequency investigation (*cf.* Fig. 4f). A linear viscoelastic region (LVER) can be observed up to 1.7% of strain (yield stress, T_y) and the crossover point (yield point, T_f) around 14.43 ± 2.63% of strain, showing a much broader region compared to the self-healing hydrogel developed previously in our group using SF as the precursor (0.1%–1.3%).[6] Therefore, the hydrogel SFO-SSDopa-Cu^{2+}-TA can bear more stress with a wider working regime. The dynamic recovery of hydrogel SFO-SSDopa-Cu^{2+}-TA is proved by continuous-step strain measurement (*cf.* Fig. 4g and h). The network structure was destroyed consecutively under crescent high strain (50–300%), but after 300 seconds of recovery time, the hydrogel always regained its gel-like properties with a higher storage modulus ($G' > G''$ at 1% strain). This reflects the contribution of many dynamic non-covalent bonds in the hydrogel network, such as metal chelation, π–π interactions, and hydrogen bonding, which are re-formed after the interface contact again. The cyclic test showed a good self-healing effect in all 6 rounds. For example, in the 3rd cyclic after the application of 150% of strain the hydrogels recovered around 90.33 ± 8.51%, and notably after the 6th consecutive cyclic test (this increased to 300% of strain), the recovery of the hydrogel could still reach 72.27 ± 9.35%, indicating the reversibility and stability of the hydrogel under this dynamic physical cross-linking.

A representative stress–strain curve (*cf.* Fig. 4i) obtained from compressive mechanical testing shows that the hydrogels begin to exhibit structural deformation at approximately 24% strain and 0.8 kPa stress (as illustrated in the schematic), which we interpret as the first indication of structural failure, albeit minimal. The compressive Young's modulus was measured at 1.72 ± 1.25 kPa, and at 40% strain, the modulus was 0.85 ± 0.39 kPa. Furthermore, the ultimate compressive strength reached 4.73 ± 1.43 kPa, and the toughness was determined to be 0.982 ± 0.34 kJ m^{-3}.

3.3 Evaluation of hydrogel adhesion capacity

The developed adhesive hydrogel is aimed to be used in bone-repairing applications; consequently, its bonding effect on different tissues is essential. Thus, firstly two adhesiveness qualitative tests were performed by using an *ex vivo* test of chicken bone with the adhesive hydrogel SFO-SSDopa-Cu^{2+}-TA. Moreover, beforehand to mimic a biological environment, the chicken bones were placed at 37 °C for 3 h. The first qualitative evaluation was based on the reconstruction of broken bone fractures, so the fragmented bone pieces were directly glued by the hydrogel, and when lifted no sign of detachment was detected, showing the potential of the hydrogel as a bone adhesive (*cf.* Fig. 5a). The second qualitative evaluation was based on perforating injury/defect simulation. For this, the penetration hole was filled with hydrogel to block leakage, and under the submission of water washings, confirmed stability under a wet environment (*cf.* Fig. 5b). In addition to the qualitative *ex vivo* direct bone adhesion, gelatin (Gel) and Hap/Gel-coated metal sheets were used to simulate tissue and bone respectively. The metal sheets were sandwiched with adhesive hydrogel at different formulations. After being placed in a humidified environment at 37 °C for 3 h and cooled down, the sample lifted 50 g of water bottle (*cf.* Fig. S8a†), confirming further its adhesive effect. For the quantitative assessment of adhesiveness, lap-shear tests were conducted (*cf.* Fig. 5c–e) using various hydrogel formulations on Gel and Hap&Gel substrates. These tests evaluated the detachment force (*cf.* Fig. S8b†), work of adhesion (*cf.* Fig. 5f), and adhesion strength (*cf.* Fig. 5g). Results showed that all hydrogel formulations exhibited significantly higher adhesive strength compared to the control group, regardless of whether the substrate was Gel or Hap&Gel. Notably, formulations containing TA demonstrated the strongest adhesive performance. This enhanced adhesion is attributed to the abundant pyrogallol (polyphenol) groups in TA, which promote additional covalent bonding with amine or thiol groups on the gelatin chains. The hydrogel SFO-SSDopa-Cu^{2+}-TA exhibited the highest performance, reaching an adhesion strength of 664.03 ± 15.87 kPa on the Gel surface and up to 854.15 ± 12.90 kPa on the Hap & Gel substrate. This improvement arises from the synergistic effects of Cu^{2+} and TA, which contribute not only to stronger interfacial adhesion but also to enhanced internal cohesion of the hydrogel network. Interestingly, the Hap & Gel surface alone (without hydrogel) showed lower adhesion strength than the Gel surface. However, when hydrogel was applied, all formulations demonstrated greater adhesion on the Hap & Gel surface. This may be attributed to the calcium ions (Ca^{2+}) in HAp, which can further participate in metal–ligand coordination within the hydrogel, enhancing adhesive interactions.

3.4 NIR laser triggered photothermal conversion and *in vitro* bone cancer ablation

Photothermal therapy is a reliable non-invasive approach in the treatment of osteosarcoma. Usually, nanoparticles are integrated into biomaterials to achieve effectiveness (>45 °C). Although the hydrogel samples developed in this study do not contain nanoparticles with photothermal properties, they are rich in catechol groups that can easily be oxidized and form metal-chelating, resulting in hydrogels in black-brown color. Such a dark color in hydrogel can make the materials responsive to NIR light to generate heat for selective tumor cell ablations.

In this study, the different ratios of SFO and SSDopa which slightly lead to the difference in the color of samples were tested. The samples were irradiated with the NIR photons (808 nm) and the average temperature was recorded to investigate their photothermal effect. To assess this, the photothermal activity of the adhesive hydrogel with a SFO SSDopa = 1 : 0.3 under different laser power densities (0.3, 0.4, 0.45, 0.5 W cm^{-2}) in a dry environment (in the air) was firstly tested (*cf.*

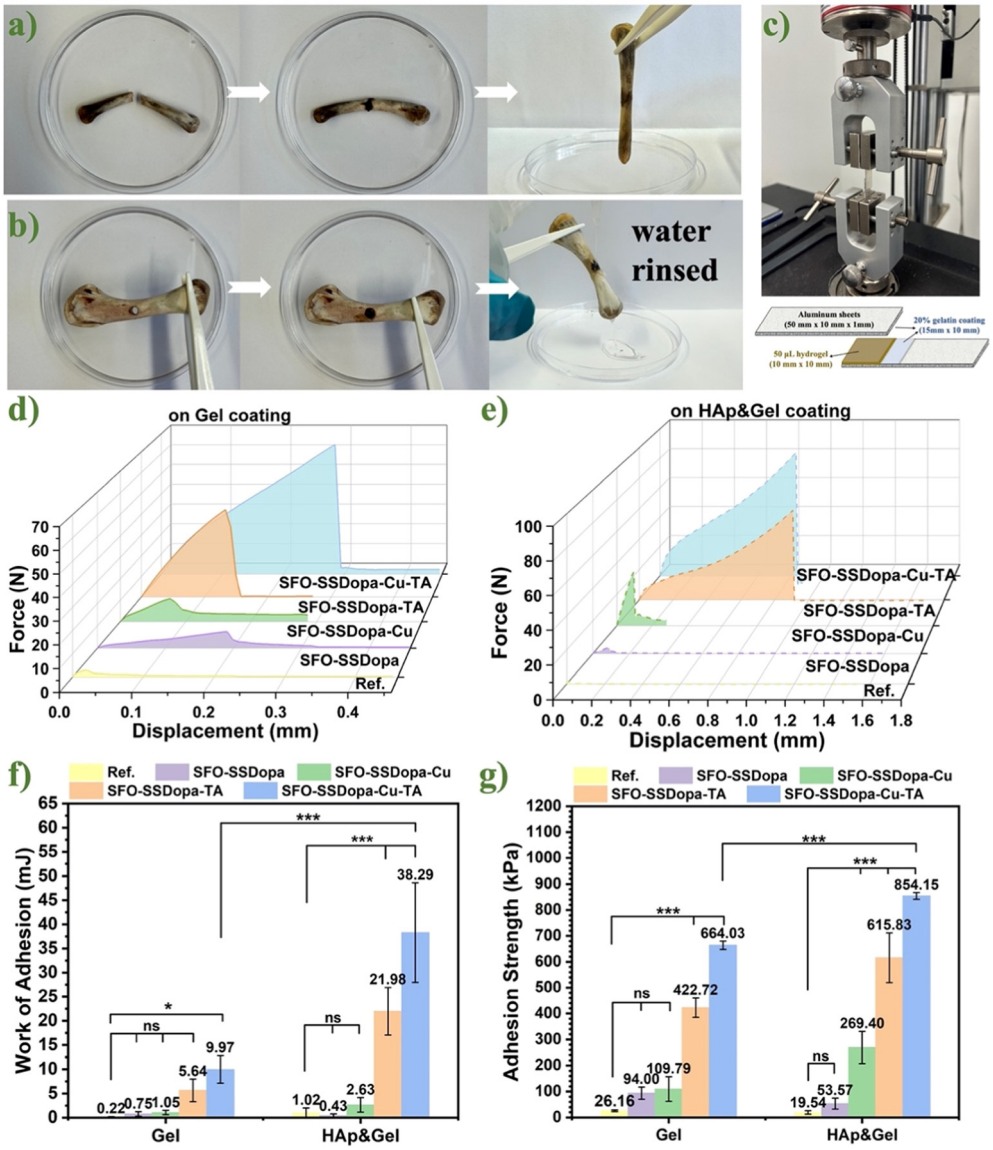

Fig. 5 Digital camera images of adhesive hydrogel SFO-SSDopa-Cu^{2+}-TA (a) binding the broken chicken bone and (b) blocking the penetration hole. (c) Preparation and stretching process of adhesive samples. Force–displacement curves in the lap shear test of different formulations on (d) Gel (20%)-based surface and (e) Hap (14%) & Gel (6%)-based surface. (f) The work of adhesion and (g) adhesive strength of hydrogel samples with different formulations compared to the control group (reference sample with only Gel or Hap & Gel coating on metal slides). * $p < 0.05$, ** $p < 0.01$ and *** $p < 0.001$ indicate the statistical significance between compared groups. $n = 3$ replicates.

Fig. 6a). The temperature rose very quickly and reached equilibrium under laser irradiation. When the power reached 0.45 W cm^{-2}, the surface temperature of the sample SFO1-SSDopa0.3-Cu^{2+}-TA reached 46–47 °C, meeting the temperature requirements for PTT. When the power density increased to 0.5 W cm^{-2}, the temperature reached above 70 °C, which was too high for *in vivo*. Therefore, in the subsequent sample analyses with different ratios of SFO/SSDopa in the air, a power density of 0.45 W cm^{-2} was selected (*cf.* Fig. 6b and S9†). All samples showed the photothermal conversion property (45–48 °C) that can be explored for PTT applications, except for that hydrogel containing SFO-only. This is due to the fact that fewer catechol groups are present in SFO compared to SSDopa, and the sample appears light yellowish brown (with less NIR absorbance) compared to dark brown-black color. Notably, in hydrogel SFO1.3-SSDopa0-Cu^{2+}-TA, although there is also no SSDopa, it contains TA in the network which is rich in phenolic hydroxyl groups, consequently this contributes to the hydrogels also having good photothermal conversion effects. Therefore, the presence of catechol groups along with the possibility of building Cu^{2+}-catecholate bonding that brings dark color to the hydrogel plays a key role in the PTT effect.

Subsequently, similar tests were conducted in a wet environment (in PBS). At this point, for hydrogel SFO1-

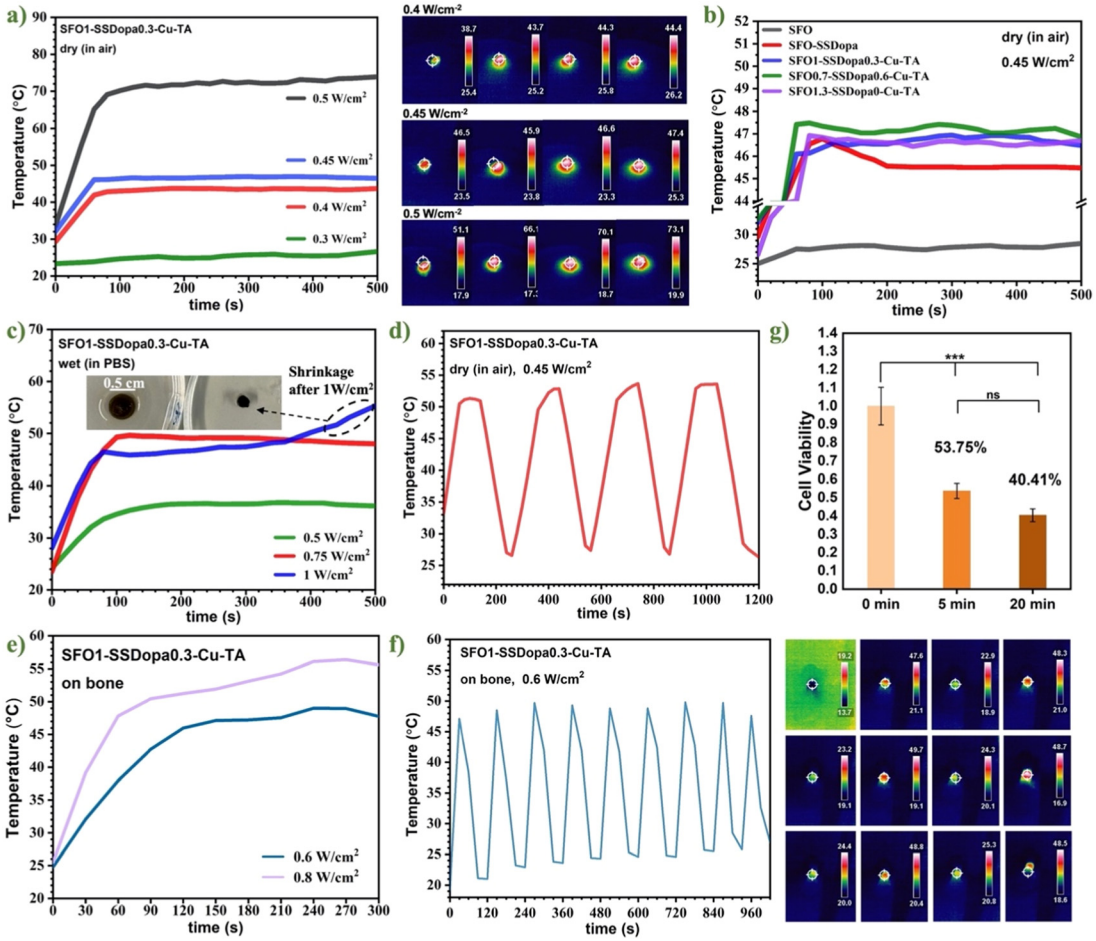

Fig. 6 (a) Evaluation of the photothermal efficacy of SFO1-SSDopa0.3-Cu^{2+}-TA irradiated by 808 nm laser with different power densities in the dry environment (in the air) with images from a thermal camera showing the surface temperature of the sample under various power densities. (b) Assessment of the PTT efficacy of hydrogel samples with different ratios of SFO/SSDopa irradiated by 808 nm laser with 0.45 W cm^{-2} power densities in the dry environment. (c) Photothermal property of SFO1-SSDopa0.3-Cu^{2+}-TA irradiated by 808 nm laser with different power densities in the wet environment (in PBS). (d) Investigation into the photothermal robustness of hydrogel SFO1-SSDopa0.3-Cu^{2+}-TA under cyclic process at 0.45 W cm^{-2} power density in the air. (e) Photothermal efficacy on representative hydrogel SFO-SSDopa-Cu^{2+}-TA by 808 nm laser with different power densities on bone. (f) Photothermal stability of hydrogel SFO1-SSDopa0.3-Cu^{2+}-TA under cyclic process at 0.6 W cm^{-2} power density on bone. (g) Cell viability of bone cancer cells MG63 after *in vitro* PTT treatment with hydrogel SFO-SSDopa-Cu^{2+}-TA under laser irradiation for 0, 5, 20 min at power density: 0.75 W cm^{-2}.

SSDopa0.3-Cu^{2+}-TA, a higher power density (0.75 W cm^{-2}) is required to reach above 40 °C (*cf.* Fig. 6c). Because, the air itself is a good flame retardant that can isolate temperature transfer and maintain heat concentration,[53,54] while in a wet environment, heat diffuses in the liquid and sometimes causes the liquid to evaporate. This is also the phenomenon demonstrated in the testing at high power density, as it is found that the volume of hydrogel shrinks significantly after 1 W cm^{-2} irradiation. Apart from that liquid acts as a barrier for NIR light as the photon can be partly absorbed and diffracted in the wet environment of hydrogels. Therefore, 0.75 W cm^{-2} power density was used for subsequent testing of samples with different ratios of SFO/SSDopa in wet environments of hydrogel (*cf.* Fig. S10†), showing that these samples containing a higher ratio of SSDopa can reach 46–50 °C with good photothermal conversion.

The photothermal durability of the representative hydrogel SFO1-SSDopa0.3-Cu^{2+}-TA was explored in a further step. On–off cyclic irradiation (on = 3 min, and off = 2 min) under 808 nm NIR laser with 0.45 W cm^{-2} power density was conducted in the air for 20 min total. When the sample was exposed to four on–off cycles, it could reach a high temperature (around 50 °C) and remain stable each time (*cf.* Fig. 6d), indicating that the hydrogel had excellent photothermal stability and could be used repeatedly.

Since this hydrogel adhesive is primarily designed for bone bonding and repair, photothermal characterization was performed not only in air and PBS environments but also directly on chicken bone tissue. Temperature changes were monitored under various laser power densities as well as during on–off cyclic irradiation to assess performance and stability.

When the representative hydrogel SFO-SSDopa-Cu^{2+}-TA was applied to the bone surface, it rapidly reached temperatures exceeding 45 °C under an irradiation power density of 0.6 W cm^{-2} (*cf.* Fig. 6e). On–off cyclic irradiation tests confirmed the photothermal stability of the hydrogel on bone tissue (*cf.* Fig. 6f). Notably, with increasing cycle numbers, a slight temperature accumulation was observed, resulting in a modest rise in the minimum temperature—indicating some degree of thermal buildup within both the hydrogel and the underlying bone.

Finally, the results of the photothermal evaluation further proved the possibility of SFO-SSDopa-Cu^{2+}-TA hydrogel used in targeted PTT therapy of osteosarcoma. Osteosarcoma cells line MG-63 were inoculated with the addition of hydrogel discs and irradiated with 808 nm laser for 0, 5, and 20 min for ablation. After irradiation, the remaining cell activity was measured by CCK8 assay. Compared with the control group with no irradiation, only 5 min of stimulation can ablate 46.25% of cancer cells, while the viability of cancer cells is only 40.41% after being irradiated for 20 min (*cf.* Fig. 6g). This proves that this hydrogel adhesive has exceptional efficiency in photothermal ablation of osteosarcoma.

3.5 *In vitro* evaluation of biocompatibility and biodegradation performance

The adhesive hydrogel used in bone tissue engineering needs to have good biocompatibility, proliferation, and migration of osteoblasts and appropriate biodegradability. For this reason, we used typical preosteoblast cell line MC3T3-E1 to analyze the biocompatibility of adhesive hydrogels in indirect assay in both 2D and 3D co-culture methods, as well as for cell migration studies. In the indirect assays, the conditioned medium was obtained by soaking the hydrogels in the culture medium at low concentrations (20 mg mL^{-1}) for 1, 3, 5, and 7 days. Then, the MC3T3-E1 cells were incubated with conditioned media of different durations for 24 hours, and afterward, their viability was measured by CCK8 assay. It can be noticed the samples did not indicate significant toxicity after culturing for 24 h (*cf.* Fig. 7a). In order to test the effect of a higher concentration of hydrogels conditioned medium and longer incubation time on cells, the culture medium soaked with hydrogels (100 mg mL^{-1}, soaking 7 days) was used to incubate cells for 24 and 72 hours. Here, all samples demonstrated good cell viability (*cf.* Fig. 7b), except for SFO-SSDopa-Cu^{2+} which can be attributed to the release of copper ions. Conversely, when the hydrogel contains TA, the phenolic hydroxyl groups in the TA structure have the ability to chelate with Cu^{2+}, thus reducing the release of these ions. At the same time, the antibacterial and anti-inflammatory properties of TA itself make the final representative SFO-SSDopa-Cu^{2+}-TA hydrogel non-toxic for osteoblastic cells and assist their proliferation after 72 h.

For a more direct evaluation of the attachment and proliferation of MC3T3-E1 cells on the hydrogel, the cells were seeded on the surface of the hydrogel and their viability was assessed at 1, 3, and 5 days by a fluorescence microscope after live–dead staining approach. As observed in the fluorescence images for SFO-SSDopa-Cu^{2+}-TA (*cf.* Fig. 7d), the cells attached to the hydrogel's surface presented good viability after day 1 and proliferated significantly after day 3 and day 5. On the 5^{th} day, many dead cells were also observed and some of them overlapped with live-stained cells after merging. It is hypothesized that this is due to the limited space for cell growth, where the later proliferating cells had no space to attach for living. Overall, the preosteoblast MC3T3-E1 cells showed a tendency of adhesion and proliferation on the adhesive hydrogel developed in this study.

Aiming to test the possibility of the developed hydrogel on the cell encapsulation, delivery, and 3D bio-printability, the MC3T3-E1 cells were encapsulated into the gel system, creating a potential BioInk. For this, the hydrogel's precursor solutions and other components were directly mixed with the cells in the culture medium and gelated in the incubator together. Most of the samples became gel after 24 h, except SFO as previously mentioned in the part of gelation time (*cf.* Fig. 3a). As presented in the CCK8 assessment (*cf.* Fig. 7c), the cell viability in SFO was very high. This is because the long gelation time of SFO (more than 8 days) enables cells to attach to the bottom and grow in the medium rather than in the hydrogel network as a 3D culturing method. In the other samples became gel in a short time, cells still have certain viability. Although it was not as expected, because the precursor solution could not be washed before use like the modeled hydrogel, it still increased the possibility of modification and other applications of this hydrogel adhesive.

Additionally, cell migration plays a crucial role in the tissue healing process by exploring the tissue environment, finding pathways, and generating traction.[55] Although scratch tests are often tested in wound healing and less in bone regeneration. However, since the adhesive hydrogel developed in this work has a good bonding effect in both bone and tissue layers (gelatin coating), adhesion of surrounding soft tissues can also support bone healing. Meanwhile, the migration of cells in the osteoblast lineage (including preosteoblasts and osteoblasts) is believed to affect bone formation.[56] Therefore, in this experiment, the migration ability of preosteoblast MC3T3-E1 cells is worth exploring as an evaluation for bone repair. Here, after a physical gap was created in the cell layer by the culture insert the conditioned medium from hydrogel extracts (20 mg mL^{-1}, collected after 5 days of soaking) was added, and monitor their movements for 24 hours under *Leica* microscopy. According to the comparison of the microscope images taken at 0, 6, 12, and 24 h (*cf.* Fig. 7e), it was found that the conditioned media extracted from hydrogels demonstrated a better ability to promote cell migration than the normal medium as the control. This is because SF and SS themselves can initiate cell migration by activating the MEK, JNK, and PI3K signaling pathways ending in c-Jun activation.[55] Although the effect of sample SFO-SSDopa-TA seems to be the best (*cf.* Fig. S10†), the hydrogel SFO-SSDopa-Cu^{2+}-TA that was finally used as an adhesive also showed excellent stimulation migration ability to help wound healing and bone regeneration.

Ultimately, bio-adhesives are typically required to have good biodegradability to ensure that materials are replaced by new

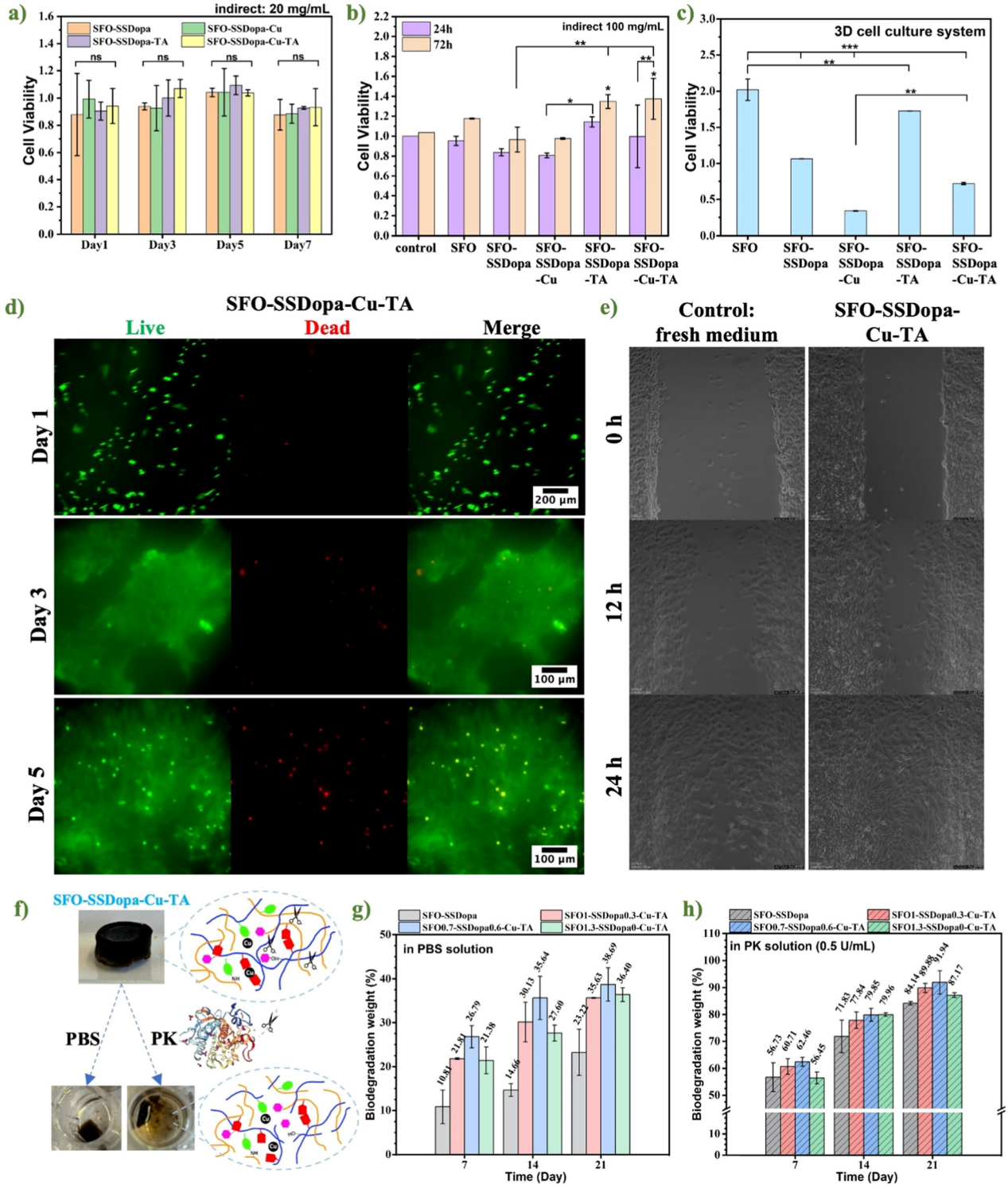

Fig. 7 (a) Evaluation of cell viability of the preosteoblastic MC3T3-E1 cells through an indirect way, after culturing in low concentration (20 mg mL^{-1}) hydrogel extracts collected at different time points (1, 3, 5, 7 days) for 24 h. (b) Cell viability and proliferation after 24 and 72 h of culture in high concentration (100 mg mL^{-1}) hydrogel extract collected after 7 days. (c) Cell viability of MC3T3-E1 cells in a hydrogel network through a 3D culture method. Statistical significance was set at: $*p < 0.05$, $**p < 0.01$ and $***p < 0.001$. (d) Fluorescence images of MC3T3-E1 cells on the hydrogel adhesive SFO-SSDopa-Cu^{2+}-TA after 1, 3, and 5 days. Live cells were stained with calcein-AM in green, while dead cells were stained with propidium iodide (PI) in red. (e) Dynamic monitoring images (0, 6, 12, and 24 h) of migration of MC3T3-E1 cell in the fresh medium as control and hydrogel extracts (20 mg mL^{-1}, collected after 5 days soaking) of different components. (f) Biodegradation of hydrogel SDO-SSDopa-Cu^{2+}-TA in different media, PBS, and PK (0.5 U mL^{-1}). (g) Biodegradation (weight loss) of hydrogel adhesives SFO-SSDopa-Cu^{2+}-TA with different ratios of SFO/SSDopa in PBS solution, and (h) in PK (0.5 unit per mL) solution. $n = 3$ replicates.

functional tissues within an acceptable time range and do not produce harmful by-products. The developed hydrogel adhesive is primarily composed of two types of silk proteins and TA. Therefore, its degradation products are expected to include peptides and amino acids from the breakdown of silk proteins,[57] as well as carboxylic acids resulting from the degradation of TA.[58] In this experiment, the aerogels with different compositions were incubated in PBS and PK (proteolytic enzyme) solutions at 37 °C. The weight loss at each time interval (7, 14, 21 days) was recorded to evaluate the degradation of the samples. In PBS solution (*cf.* Fig. 7g), the biodegradation rate of samples could reach about 30% after 21 days, which is higher than the degradation of chemical-crosslinked SF hydrogel.[6,12] The abundant dynamic interactions in networks and hydrophilic content: SSDopa and TA, contributed to the easier entry of PBS. In the PK solution (*cf.* Fig. 7h), the biodegradation of the samples after 21 days is all over 84%, much higher than that of PBS. This is because PK, as a proteolytic enzyme, can cleave peptide bonds near the carboxyl groups and aromatic amino acids in silk protein chains,[59] enabling rapid dissolution and degradation of the samples (*cf.* Fig. 7f). Finally, the biodegradation of adhesive hydrogel SFO-SSDopa-Cu^{2+}-TA in PBS or PBS/PK increased gradually with time extension and showed excellent degradation ability in PK after 21 days.

4. Conclusions

In summary, in this work, we took advantage of two different silk-derived proteins (SF and SS) to interactively create injectable adhesive hydrogel systems (SFO-SSDopa-Cu^{2+}-TA-based hydrogels), to help bone repair with the ability of photothermal ablation of bone cancer cells. SFO and SSDopa were produced by introducing catechol groups into SF and SS chains through different methods, enabling the hydrogel network to exhibit excellent shear-thinning properties and self-healing capabilities. These characteristics were facilitated by various catechol cross-linking interactions and reversible physical cross-linking after chelation with copper ions. At the same time, this hydrogel has excellent adhesion to bone and underlying soft tissues for repairing bone injury. Under 808 nm NIR irradiation, the hydrogel reached a temperature of 45–48 °C meeting the requirement for photothermal therapy of bone cancer cells, as well as maintaining the stability of photothermal conversion in the cyclical test. Under the excitation of 5 and 20 minutes, the targeted photothermal effect of hydrogel showed excellent osteosarcoma cell ablation ability. In the biocompatibility evaluation, the low and high concentrations soaking medium of the hydrogel did not show any cytotoxicity to preosteoblast MC3T3-E1 cells, and the cells could attach to the hydrogel and proliferate in large numbers after 3 days. Cells can also survive in the hydrogel network in the co-culture system, which provides the possibility of hydrogel encapsulation of cells for building 3D printing BioInks. The injectability, excellent self-healing ability, robust bone/tissue adhesion ability, effective PTT performance, proper biodegradation, and good biocompatibility of SFO-SSDopa-Cu^{2+}-TA make it a promising bio-adhesive for bone repairing and bone cancer therapy in minimally invasive surgery paving the way for clinical translation.

Data availability

The data supporting this article have been included as part of the ESI.†

Conflicts of interest

There are no conflicts to declare.

Acknowledgements

H. M. and G. S. acknowledge the support of the German Research Foundation (DFG, Projektnummer 467116484 to H. M. as well as 397484323, 468236352, and 384170921 to G. S.) and the Centre of Molecular Medicine Cologne for financial assistance. S. C. acknowledges Sumiya Iqbal and Niusha Heshmati in the Research group of Prof. Sanjay Mathur for analysis supports.

References

1 S. Gil, I. Fernandez-Pineda, B. Rao, M. D. Neel, J. N. Baker, H. Wu, J. Wu and D. L. Anghelescu, *Am. J. Hosp. Palliat. Care*, 2019, **36**, 105–110.
2 Mayo Clinic Press, **https://order.store.mayoclinic.com/flex/mmv/fhblc01/?altkey=FHBORG&utm_source=MC-DotOrg-PS&utm_medium=Link&utm_campaign=FamilyHealth-Book&utm_content=FHB**, (accessed September 19, 2024).
3 H. Zhang, S. Wu, W. Chen, Y. Hu, Z. Geng and J. Su, *Bioact. Mater.*, 2023, **23**, 156–169.
4 H. C. Pape, A. Evans and P. Kobbe, *J. Orthop. Trauma*, 2010, **24**(Suppl 1), S36–S40.
5 N. Abie, C. Ünlü, A. R. Pinho, M. C. Gomes, T. Remmler, M. Herb, D. Grumme, E. Tabesh, M.-A. Shahbazi, S. Mathur, J. F. Mano and H. Maleki, *ACS Appl. Mater. Interfaces*, 2024, **18**, 22809–22827.
6 H. K. Pektas, Y. Demidov, A. Ahvan, N. Abie, V. S. Georgieva, S. Chen, S. Farè, B. Brachvogel, S. Mathur and H. Maleki, *ACS Mater. Au*, 2023, **3**, 711–726.
7 M. Donkerwolcke, F. Burny and D. Muster, *Biomaterials*, 1998, **19**, 1461–1466.
8 L. Liu, Y. Xiang, Z. Wang, X. Yang, X. Yu, Y. Lu, L. Deng and W. Cui, *NPG Asia Mater.*, 2019, **11**, 1–18.
9 S. Lü, X. Bai, H. Liu, P. Ning, Z. Wang, C. Gao, B. Ni and M. Liu, *J. Mater. Chem. B*, 2017, **5**, 3739–3748.
10 D. N. Céspedes-Valenzuela, S. Sánchez-Rentería, J. Cifuentes, M. Gantiva-Diaz, J. A. Serna, L. H. Reyes,

C. Ostos, C. Cifuentes-De la Portilla, C. Muñoz-Camargo and J. C. Cruz, *Polymers*, 2021, **14**, 126.
11 K. Lei, Q. Zhu, X. Wang, H. Xiao and Z. Zheng, *ACS Biomater. Sci. Eng.*, 2019, **5**, 5489–5497.
12 N. Al-Jawuschi, S. Chen, N. Abie, T. Fischer, S. Fare and H. H. Maleki, *Langmuir*, 2023, **39**, 4326–4337.
13 S. Guo, D. Gu, Y. Yang, J. Tian and X. Chen, *J. Nanobiotechnol.*, 2023, **21**, 348.
14 Z. Yu, H. Wang, B. Ying, X. Mei, D. Zeng, S. Liu, W. Qu, X. Pan, S. Pu, R. Li and Y. Qin, *Mater. Today Bio*, 2023, **23**, 100834.
15 L. Zhao, X. Zhang, X. Wang, X. Guan, W. Zhang and J. Ma, *J. Nanobiotechnol.*, 2021, **19**, 335.
16 N. Mauro, M. A. Utzeri, P. Varvarà and G. Cavallaro, *Molecules*, 2021, **26**, 3085.
17 Y. Zhang, R. Ning, W. Wang, Y. Zhou and Y. Chen, *Front. Bioeng. Biotechnol.*, 2022, **10**, 844540.
18 J. Shi, J. Li, Y. Wang, J. Cheng and C. Y. Zhang, *J. Mater. Chem. B*, 2020, **8**, 5793–5807.
19 Y. Liu, K. Ai, J. Liu, M. Deng, Y. He and L. Lu, *Adv. Mater.*, 2013, **25**, 1353–1359.
20 E. I. Shramova, A. B. Kotlyar, E. N. Lebedenko, S. M. Deyev and G. M. Proshkina, *Acta Nat.*, 2020, **12**, 102–113.
21 A. Reizabal, A. Fidalgo-Marijuan, R. Gonçalves, A. Gutiérrez-Pardo, F. Aguesse, L. Pérez-Álvarez, J. L. Vilas-Vilela, C. M. Costa and S. Lanceros-Mendez, *J. Colloid Interface Sci.*, 2022, **611**, 366–376.
22 J. K. Sahoo, O. Hasturk, T. Falcucci and D. L. Kaplan, *Nat. Rev. Chem.*, 2023, **7**, 302–318.
23 S. Tharakan, I. Raja, A. Pietraru, E. Sarecha, A. Gresita, E. Petcu, A. Ilyas and M. Hadjiargyrou, *Gels*, 2023, **9**, 274.
24 Y. Lu, X. Huang, Y. Luo, R. Zhu, M. Zheng, J. Yang and S. Bai, *Biomacromolecules*, 2023, **24**, 319–331.
25 E. Khalatbari, M. Tajabadi and A. Khavandi, *Mater. Today Commun.*, 2022, **31**, 103549.
26 X. Tang, W. Wu, S. Zhang, C. He, K. Fan, Y. Fan, X. Yang, J. Li, Y. Yang and J. Ling, *Biomater. Sci.*, 2025, **13**, 606–616.
27 X. Gu, X. Chen, X. Tang, Z. Zhou, T. Huang, Y. Yang and J. Ling, *Nanotechnol. Rev.*, 2021, **10**, 10–19.
28 X. Chen, X. Tang, Y. Wang, X. Gu, T. Huang, Y. Yang and J. Ling, *Biomater. Adv.*, 2022, **135**, 112674.
29 M. A. Serban, B. Panilaitis and D. L. Kaplan, *J. Biomed. Mater. Res., Part A*, 2011, **98A**, 567–575.
30 K. A. Burke, D. C. Roberts and D. L. Kaplan, *Biomacromolecules*, 2016, **17**, 237–245.
31 X. Gao, Q. Dai, L. Yao, H. Dong, Q. Li and X. Cao, *Biomater. Sci.*, 2020, **8**, 2694–2701.
32 H. Zheng, N. Lin, Y. He and B. Zuo, *ACS Appl. Mater. Interfaces*, 2021, **13**, 40013–40031.
33 J.-W. Seo, H. Kim, K. Kim, S. Q. Choi and H. J. Lee, *Adv. Funct. Mater.*, 2018, **28**, 1800802.
34 A. Z. Siavashani, J. Mohammadi, M. Rottmar, B. Senturk, J. Nourmohammadi, B. Sadeghi, L. Huber and K. Maniura-Weber, *Int. J. Biol. Macromol.*, 2020, **153**, 317–326.
35 S.-J. Seo, G. Das, H.-S. Shin and J. K. Patra, *Int. J. Mol. Sci.*, 2023, **24**, 4951.
36 Y. Zhang, R. Sheng, J. Chen, H. Wang, Y. Zhu, Z. Cao, X. Zhao, Z. Wang, C. Liu, Z. Chen, P. Zhang, B. Kuang, H. Zheng, C. Shen, Q. Yao and W. Zhang, *Adv. Mater.*, 2023, **35**, 2210517.
37 R. I. Kunz, R. M. C. Brancalhão, L. de F. C. Ribeiro and M. R. M. Natali, *BioMed. Res. Int.*, 2016, **2016**, 8175701.
38 Genoa Blankenship, 2023.
39 T. Priemel, G. Palia, F. Förste, F. Jehle, S. Sviben, I. Mantouvalou, P. Zaslansky, L. Bertinetti and M. J. Harrington, *Science*, 2021, **374**, 206–211.
40 B. Jayachandran, T. Parvin, M. Alam, K. Chanda and B. Musuvathi, *Molecules*, 2022, **27**, 8124.
41 Z. Zheng, S. Guo, Y. Liu, J. Wu, G. Li, M. Liu, X. Wang and D. Kaplan, *J. Biomater. Appl.*, 2016, **31**, 450–463.
42 J. P. Kumar, N. Bhardwaj and B. B. Mandal, *RSC Adv.*, 2016, **6**, 105125–105136.
43 C. Yan, J. Liang, H. Fang, X. Meng, J. Chen, Z. Zhong, Q. Liu, H. Hu and X. Zhang, *Gels*, 2021, **7**, 23.
44 Hydroxyapatite, **https://www.acs.org/molecule-of-the-week/archive/h/hydroxyapatite.html**, (accessed March 3, 2025).
45 A. J. Dominijanni, M. Devarasetty, S. D. Forsythe, K. I. Votanopoulos and S. Soker, *Tissue Eng., Part C*, 2021, **27**, 401–410.
46 K. S. Lim, J. Kundu, A. Reeves, L. A. Poole-Warren, S. C. Kundu and P. J. Martens, *Macromol. Biosci.*, 2012, **12**, 322–332.
47 H. Rahmani, A. Fattahi, K. Sadrjavadi, S. Khaledian and Y. Shokoohinia, *Adv. Pharm. Bull.*, 2019, **9**, 601–608.
48 J. Saha, Md. I. H. Mondal, Md. R. Karim Sheikh and Md. A. Habib, *J. Textile Sci. Eng.*, 2019, **9**(1), 1–5.
49 M. Paolieri, Z. Chen, F. Babu Kadumudi, M. Alehosseini, M. Zorrón, A. Dolatshahi-Pirouz and H. Maleki, *ACS Appl. Nano Mater.*, 2023, **6**, 5211–5223.
50 F. Sousa, G. M. Guebitz and V. Kokol, *Process Biochem.*, 2009, **44**, 749–756.
51 L. Kafi-Ahmadi and B. Javanpour, *React. Kinet., Mech. Catal.*, 2020, **130**, 935–954.
52 Z. Yin, H. Liu, M. Lin, W. Xie, X. Yang and Y. Cai, *Biomed. Mater.*, 2021, **16**, 045025.
53 I. van der Veen and J. de Boer, *Chemosphere*, 2012, **88**, 1119–1153.
54 A. G. Shmakov, O. P. Korobeinichev, A. M. Mebel, D. P. Porfiriev, A. R. Ghildina, K. N. Osipova, D. A. Knyazkov, I. E. Gerasimov, Z. Liu and B. Yang, *Combust. Flame*, 2023, **249**, 112614.
55 C. Martínez-Mora, A. Mrowiec, E. M. García-Vizcaíno, A. Alcaraz, J. L. Cenis and F. J. Nicolás, *PLoS One*, 2012, **7**, e42271.
56 S. Aryal, A. C. S. Aryal, K. Miyai, Y. Izu, T. Hayata, T. Notomi, M. Noda and Y. Ezura, *Proc. Natl. Acad. Sci. U. S. A.*, 2015, **112**, 15432–15437.
57 C. Guo, C. Li and D. L. Kaplan, *Biomacromolecules*, 2020, **21**, 1678–1686.
58 N. Bensalah, K. Chair and A. Bedoui, *Sustainable Environ. Res.*, 2018, **28**, 1–11.
59 W. Ebeling, N. Hennrich, M. Klockow, H. Metz, H. D. Orth and H. Lang, *Eur. J. Biochem.*, 1974, **47**, 91–97.